MASARYKOVA UNIVERZITA
PŘÍRODOVĚDECKÁ FAKULTA
ÚSTAV TEORETICKÉ FYZIKY A ASTROFYZIKY

Bakalářská práce

BRNO 2026 JAKUB MATULA

MASARYKOVA UNIVERZITA
PŘÍRODOVĚDECKÁ FAKULTA
ÚSTAV TEORETICKÉ FYZIKY A ASTROFYZIKY

Modelování akrece na černou díru

Bakalářská práce

Jakub Matula

Vedoucí práce: Mgr. Ing. arch. Petr Kurfürst, Ph.D. **Brno 2026**

Bibliografický záznam

Autor:	Jakub Matula Přírodovědecká fakulta, Masarykova univerzita Ústav teoretické fyziky a astrofyziky
Název práce:	Modelování akrece na černou díru
Studijní program:	Fyzika
Studijní obor:	Astrofyzika
Vedoucí práce:	Mgr. Ing. arch. Petr Kurfürst, Ph.D.
Akademický rok:	2025/2026
Počet stran:	$\mathrm{ix} + 51$
Klíčová slova:	černá díra; supermasivní černá díra; akrece; akreční disk; aktivní galaktická jádra; magnetohydrodynamika; astrofyzikální výtrysky; bipolární odtok; numerické simulace; spektrální energetická rozdělení; radiační přenos

Bibliographic Entry

Author:	Jakub Matula Faculty of Science, Masaryk University Department of theoretical physics and astrophysics
Title of Thesis:	Modelling accretion onto a black hole
Degree Programme:	Physics
Field of Study:	Astrophysics
Supervisor:	Mgr. Ing. arch. Petr Kurfürst, Ph.D.
Academic Year:	2025/2026
Number of Pages:	ix + 51
Keywords:	black hole; supermassive black hole; accretion; accretion disc; active galactic nuclei; magnetohydrodynamics; astrophysical jets; bipolar outflow; numerical simulations; spectral energy distribution; radiative transfer

Abstrakt

Tato bakalářská práce se věnuje numerickému modelování akrečního procesu na supermasivní černou díru o hmotnosti $M_\bullet = 4 \times 10^6\, M_\odot$, motivovanému pozorovanými vlastnostmi aktivních galaktických jader a systémů typu Sgr A*. Pomocí kódu *CASTRO* byla provedena dvourozměrná cylindrická hydrodynamická simulace a trojrozměrné kartézské magnetohydrodynamické (MHD) simulace pro tři různé intenzity magnetického pole. Radiační přenos byl následně modelován programem *SEDONA*. Hydrodynamická simulace ukazuje, že akreční disk zůstává po celou dobu vývoje geometricky tenký a stabilní, přičemž v oblasti vnitřní hranice vzniká bipolární vítr poháněný tepelným tlakem. Trojrozměrné MHD simulace potvrzují vznik perzistentních bipolárních výtoků ohraničených nízkohustotními polárními dutinami, přičemž konfigurace se silným polem navíc vykazuje výraznou hemisférickou asymetrii. Spektrální energetická rozdělení závislá na zorném úhlu ukazují, že polární emise je koncentrována v oblasti měkkého rentgenového záření, zatímco ekvatoriální spektra dosahují maxima v extrémním ultrafialovém oboru. Bolometrické jasnosti potvrzují silný efekt úhlové anizotropie, kdy toky v polárním směru převyšují ekvatoriální hodnoty až o řád.

Abstract

This thesis presents a numerical study of accretion onto a supermassive black hole of mass $M_\bullet = 4 \times 10^6\, M_\odot$, motivated by the observed properties of active galactic nuclei and systems such as Sgr A*. Two-dimensional cylindrical hydrodynamic and three-dimensional Cartesian magnetohydrodynamic (MHD) simulations were performed using the *CASTRO* code, followed by radiative transfer post-processing with *SEDONA*. The hydrodynamic simulation demonstrates that the accretion disc remains geometrically thin and stable throughout its evolution, while a pressure-driven bipolar wind emerges from the inner boundary region. The three-dimensional MHD simulations, conducted for three different magnetic field strengths, confirm the formation of persistent bipolar outflows bounded by low-density polar cavities, with the strong-field configuration additionally exhibiting pronounced hemispheric asymmetry. Angle-resolved spectral energy distributions show that polar emission is concentrated in the soft X-ray band, while equatorial spectra peak in the extreme ultraviolet. Bolometric luminosities confirm strong angular anisotropy, with polar fluxes exceeding equatorial values by up to an order of magnitude.

MUNI
SCI

MASARYKOVA UNIVERZITA
PŘÍRODOVĚDECKÁ FAKULTA
KOTLÁŘSKÁ 2, 611 37 BRNO
IČ: 00216224
DIČ: CZ00216224

ZADÁNÍ BAKALÁŘSKÉ PRÁCE

Akademický rok: 2025/2026

Ústav:	Ústav teoretické fyziky a astrofyziky
Student:	Jakub Matula
Program:	Fyzika
Specializace:	Astrofyzika

Ředitel *ústavu* PřF MU Vám ve smyslu Studijního a zkušebního řádu MU určuje bakalářskou práci s názvem:

Název práce:	Modelování akrece na černou díru
Název práce anglicky:	Modeling accretion onto a black hole
Jazyk práce:	angličtina

Oficiální zadání:
Accretion disks around stellar and central galactic black holes are crucial for the production of enormous amounts of energy; the manifestations of accretion can then be observed, usually at very short wavelengths. These disks very often give rise to astrophysical jets coming from the vicinity of the central object. Using established multidimensional programs and codes, we create a model of such an accretion, incorporating effects leading to the jet production. We will also calculate the observable effects of accretion on some types of black holes, in particular the total luminosity of this process and its distribution in different spectral regions.

Literatura:
FRANK, Juhan; Andrew KING a Derek J. RAINE. *Accretion power in astrophysics*. 3rd ed. Cambridge: Cambridge University Press, 2002, xiv, 384. ISBN 0521629578.

KARAS, Vladimír; Jiří SVOBODA a Michal ZAJAČEK. *Selected Chapters on Active Galactic Nuclei as Relativistic Systems*. Opava: Institute of Physics, Silesian University in Opava, 2021, 154 s. Lecture notes. ISBN 978-80-7510-475-5.

Vedoucí práce:	Mgr. Ing. arch. Petr Kurfürst, Ph.D.
Konzultant:	Bestin James, Ph.D. doc. RNDr. Michal Zajaček, Dr. rer. nat.
Datum zadání práce:	4. 4. 2025
V Brně dne:	5. 5. 2026

Zadání bylo schváleno prostřednictvím IS MU.

Jakub Matula, 21. 10. 2025
Mgr. Ing. arch. Petr Kurfürst, Ph.D., 23. 11. 2025
RNDr. Luboš Poláček, 11. 12. 2025

Poděkování

Rád bych v první řadě poděkoval svému vedoucímu bakalářské práce Mgr. Ing. arch. Petru Kurfürstovi, Ph.D., za trpělivé vedení, čas věnovaný konzultacím a za ochotu sdílet své zkušenosti s numerickým modelováním. Poděkování patří také provozovatelům výpočetní infrasktrukury Metacentum, bez jejíchž prostředků by simulace obsažené v této práci nebylo možné realizovat. Na závěr děkuji své rodině a přátelům za podporu během celého studia.

Prohlášení

Prohlašuji, že jsem svoji bakalářskou práci vypracoval samostatně pod vedením vedoucího práce s využitím informačních zdrojů, které jsou v práci citovány.

Brno 13. května 2026 ....

Jakub Matula

Contents

Chapter 1

Black holes, accretion and jets

1.1 Black holes

1.1.1 Definition, basic properties, and formation

A black hole is a region of spacetime where the gravitational field is so strong that neither matter nor light can escape to infinity. The boundary of this region is called the event horizon, which acts as a one-way surface: matter and radiation can cross it inward, but nothing can travel outward through it. For a non-rotating black hole of mass $M_\bullet$, the event horizon is located at the Schwarzschild radius [Schwarzschild, 1916],

$$r_\mathrm{s} = \frac{2GM_\bullet}{c^2}, \tag{1.1}$$

where G is the gravitational constant and c is the speed of light. Unlike a neutron star or a white dwarf, a black hole has no physical surface at r_s. Once matter crosses the event horizon, it is causally disconnected from the rest of the universe, and the black hole's presence can only be detected through the gravitational field it produces [Frank et al., 2002].

An important result from general relativity, known as the no-hair theorem, states that a black hole in its final state is completely described by just two quantities: its mass $M_\bullet$ and its angular momentum J. All other properties of the original collapsing body are radiated away as gravitational waves during the formation process [Frank et al., 2002].

Black holes of stellar mass form when a massive star exhausts its nuclear fuel and can no longer support itself against its own gravity. Oppenheimer and Snyder [1939] showed that if the mass of the collapsing core is too large to be supported by neutron degeneracy pressure, the collapse continues without limit. From the point of view of a distant observer, the surface of the star approaches the Schwarzschild radius asymptotically, with light from the surface becoming increasingly redshifted. However, an observer falling with the collapsing matter crosses the event horizon in finite proper time. Because real stars rotate, the final product of such a collapse is, in general, a rotating black hole described by the Kerr solution [Frank et al., 2002], which we discuss in Section 1.1.2.

1.1.2 Classification – Schwarzschild and Kerr black holes

The simplest solution to Einstein's field equations regarding black holes is the Schwarzschild metric [Schwarzschild, 1916]. This solution describes a non-rotating, electrically neutral black hole that is characterised solely by its mass $M_\bullet$. In this model, the spacetime geometry is static and spherically symmetric. The event horizon is located at the Schwarzschild radius $r_\mathrm{s} = 2GM_\bullet/c^2$, as established in the previous section, and represents the boundary from which no information can escape.

In an astrophysical context, however, perfectly static black holes are unlikely to exist. Because stars possess angular momentum, which must be conserved during gravitational collapse, most astrophysical black holes are expected to rotate [Frank et al., 2002]. Such objects are described by the Kerr solution [Kerr, 1963]. This metric introduces a second parameter: the angular momentum J. To simplify the mathematical description, it is common to define the spin parameter $a = J/(M_\bullet c)$ or the dimensionless spin $a_* = ac/(GM_\bullet)$, which is restricted to the range $0 \leq a_* \leq 1$. Within this framework, the Schwarzschild solution is recovered when $a_* = 0$, while $a_* = 1$ represents a maximally rotating black hole.

The rotation of a black hole significantly alters the surrounding spacetime geometry in two primary ways. First, the location of the event horizon is no longer fixed at the Schwarzschild radius. For a Kerr black hole, the horizon moves inward as the spin increases, with its radial coordinate r_+ given by [Bardeen et al., 1972]:

$$r_+ = \frac{GM_\bullet}{c^2}\left(1 + \sqrt{1 - a_*^2}\right). \tag{1.2}$$

For a non-rotating black hole with $a_* = 0$, this reduces to the Schwarzschild radius, while for a maximally rotating black hole with $a_* = 1$, the horizon shrinks to its minimum value $GM_\bullet/c^2$.

Furthermore, rotation creates a unique region outside the event horizon known as the ergosphere. Within this volume, the rotation of the black hole drags spacetime itself — an effect known as frame dragging. This influence is so strong that no physical observer can remain stationary relative to distant stars; all matter is forced to rotate in the same direction as the black hole [Bardeen et al., 1972]. The outer boundary of the ergosphere, referred to as the static limit, is defined by:

$$r_0 = \frac{GM_\bullet}{c^2}\left(1 + \sqrt{1 - a_*^2 \cos^2\theta}\right), \tag{1.3}$$

where θ denotes the polar angle. Consequently, the ergosphere is not spherical but takes on an oblate shape that touches the event horizon at the poles and reaches its maximum extent at the equator. This region is of particular interest for energy extraction mechanisms, which are discussed in Section 1.3.2.

1.1.3 Key relativistic quantities

In the study of black hole physics, the gravitational radius r_{g} serves as a fundamental length scale. It is defined by the expression:

$$r_{\mathrm{g}} = \frac{GM_{\bullet}}{c^2}. \tag{1.4}$$

This quantity determines the characteristic scale of the spacetime curvature in the vicinity of a compact object. The Schwarzschild radius, introduced in Section 1.1.1, corresponds to $2r_{\mathrm{g}}$. Similarly, the event horizon of a Kerr black hole can be expressed compactly using equation (1.2) as $r_+ = r_{\mathrm{g}}(1 + \sqrt{1 - a_*^2})$.

A critical threshold in the dynamics of accretion is the innermost stable circular orbit, commonly referred to as the ISCO. While Newtonian mechanics allows for stable circular orbits at any radius, provided the test particle has sufficient angular momentum, general relativity introduces a limit to this stability. Below a specific radial distance, circular orbits become unstable. Any small perturbation causes a particle to spiral inward and fall into the black hole. Consequently, the ISCO defines the physical inner boundary of an accretion disc [Bardeen et al., 1972].

For a non-rotating Schwarzschild black hole, the ISCO is located at:

$$r_{\mathrm{ISCO}} = 6\, r_{\mathrm{g}}. \tag{1.5}$$

Within this radius, no stable circular motion is possible and matter must inevitably fall toward the central object. In the case of a rotating Kerr black hole, the ISCO radius becomes a function of the spin parameter a_* and the orbital orientation. For prograde orbits, where the matter rotates in the same direction as the black hole, the ISCO moves inward. In the limit of a maximally rotating black hole with $a_* = 1$, the ISCO reaches $r_{\mathrm{ISCO}} = r_{\mathrm{g}}$. In contrast, for retrograde orbits, the ISCO expands to $r_{\mathrm{ISCO}} = 9\, r_{\mathrm{g}}$ [Bardeen et al., 1972].

The dependence of the ISCO on the spin parameter has significant observational implications. The proximity of the inner edge of the accretion disc to the event horizon directly affects the efficiency of the conversion of gravitational energy into radiation. These mechanisms and their impact on total luminosity are further discussed in Section 1.2.3.

1.2 Accretion

As established in Section 1.1.1, black holes lack a physical surface, yet the conversion of gravitational potential energy during accretion represents a highly efficient process. The primary challenge in this mechanism is how the infalling gas, which typically possesses significant specific angular momentum, reaches the central object. This angular momentum prevents direct free-fall and instead forces the infalling material into orbital motion around the central mass, ultimately leading to the formation of an accretion disc, a differentially rotating structure where internal stresses transport angular momentum outward, allowing matter to spiral inward.

1.2.1 Origin of accretion – why a disc forms

In gas-rich environments, such as close binary systems with mass-losing companions or the nuclei of active galaxies, the infalling material inherently possesses a specific angular momentum. This is defined as the angular momentum per unit mass, $\ell = R^2\Omega$, where R denotes the cylindrical distance (distance from a rotation axis) from the central object and Ω represents the local angular velocity. In the absence of external torques, this angular momentum must be conserved, and this constitutes the primary barrier to direct accretion [Frank et al., 2002].

Consequently, the infalling gas cannot reach the central object directly. Instead, the material settles in a circular orbit at a characteristic radius, known as the circularization radius R_{circ}, where the centrifugal force balances the gravitational pull. For most compact objects, R_{circ} significantly exceeds the physical dimensions of the central mass. As a result, the gas initially accumulates in a ring at this radius rather than being accreted immediately [Frank et al., 2002].

Within this ring, dissipative processes, namely collisions between gas elements and shock waves, convert orbital kinetic energy into thermal energy, which is then radiated away. Because circular orbits represent the lowest energy configuration for a given angular momentum, the gas naturally settles into a disc-like structure [Pringle, 1981]. However, to migrate further inward, the material must redistribute its angular momentum. This transport is facilitated by viscous stresses acting between adjacent fluid layers rotating at different velocities. These stresses effectively transfer angular momentum outward, allowing the mass to flow toward the central black hole. The resulting structure is a geometrically thin, differentially rotating accretion disc, whose governing equations are developed in detail in the Appendix A.

1.2.2 Types of accretion discs

The best established model is the geometrically thin, optically thick accretion disc, widely known as the standard thin disc or the Shakura-Sunyaev model [Shakura and Sunyaev, 1973]. This regime occurs when the mass accretion rate $\dot{M}_\bullet$, defined as the rate at which mass flows through the disc toward the central object,

$$\dot{M}_\bullet = -2\pi R \Sigma V_R, \tag{1.6}$$

remains low enough for the disc to efficiently radiate away viscously generated heat. Here, Σ is the surface density of the disc, V_R is the radial drift velocity, and the negative sign ensures that $\dot{M}_\bullet > 0$ for the inward flow. The derivation of this expression from the continuity equation is given in Appendix A. Consequently, the disc maintains a low temperature, its vertical extent remains significantly smaller than its radial scale, and the gas motion is characterised by nearly Keplerian circular orbits.

As the accretion rate increases, radiative cooling may become insufficient to balance the rate of viscous heating. In such cases, the disc thickens vertically and radiation becomes trapped within the flow, a state described by the slim disc model [Frank et al., 2002]. Under even higher accretion rates, the structure transforms into a geometrically thick torus, where radiation pressure provides the primary support against gravity.

Conversely, at extremely low accretion rates, the gas density is reduced to the point where collisions between ions and electrons are infrequent, preventing the establishment of thermal equilibrium. This regime, known as an advection-dominated accretion flow (ADAF), is characterised by the viscously generated heat being stored within the gas and advected inward rather than radiated locally [Frank et al., 2002].

Given that the simulations performed in this work focus on the sub-Eddington, radiatively efficient regime, the thin disc approximation serves as the most suitable framework. Its governing equations and physical assumptions are developed in detail in the Appendix A.

1.2.3 Accretion luminosity and efficiency

The accretion process releases gravitational potential energy as radiation when infalling matter descends within the gravitational potential of a central object. For a central mass $M_\bullet$ and an inner disc radius $r_\bullet$ (corresponding to $r_{\rm s}$), the accretion luminosity $L_{\rm acc}$ produced by a steady mass flow $\dot{M}_\bullet$ is defined as [Frank et al., 2002]

$$L_{\rm acc} = \frac{G M_\bullet \dot{M}_\bullet}{r_\bullet}. \tag{1.7}$$

This relation indicates that the luminosity scales directly with the compactness of the accreting object, where a smaller inner radius corresponds to a more efficient release of energy.

A more general way to express the accretion luminosity incorporates the radiative efficiency parameter η,

$$L_{\rm acc} = \eta \dot{M}_\bullet c^2, \tag{1.8}$$

where η measures how efficiently the rest-mass energy of the accreted material is converted into radiation [Frank et al., 2002]. For a standard thin disc around a non-rotating Schwarzschild black hole, the inner edge of the disc is assumed to coincide with the ISCO at $r_{\rm ISCO} = 6\, r_{\rm g}$, as established in Section 1.1.3, resulting in a radiative efficiency of approximately $\eta \approx 0.06$. In contrast, for a maximally rotating Kerr black hole with $a_* = 1$, the ISCO moves inward to $r_{\rm g}$, allowing matter to descend significantly deeper into the potential well, increasing the efficiency to approximately $\eta \approx 0.40$ [Shakura and Sunyaev, 1973]. The strong dependence of η on the black hole spin is a primary factor in the astrophysical significance of the spin parameter.

At high accretion rates, the outward radiation pressure may become sufficient to counteract the inward gravitational pull. The luminosity threshold at which these forces reach equilibrium is known as the Eddington luminosity. This limit is derived by balancing the radiation pressure against the gravitational force acting on an ionised hydrogen plasma [Frank et al., 2002],

$$L_{\rm Edd} = \frac{4\pi G M_\bullet m_{\rm p} c}{\sigma_T} \approx 1.3 \times 10^{38} \left(\frac{M_\bullet}{M_\odot}\right) \ {\rm erg\ s^{-1}}, \tag{1.9}$$

where m_{p} denotes the proton mass and σ_T represents the Thomson scattering cross-section. The Eddington luminosity serves as a theoretical upper limit for steady accretion, defining the boundary between the sub-Eddington regime, where the geometrically thin disc model is applicable, and the super-Eddington regime, characterised by vertically extended structures, as discussed in Section 1.2.2.

1.3 Jets

Astrophysical jets represent some of the most energetic phenomena associated with accreting compact objects. They appear as highly collimated plasma outflows observed across a wide range of scales, from stellar-mass black holes in X-ray binaries (XRB) to supermassive black holes in active galactic nuclei (AGN). Despite the enormous difference in the mass of the central object, the physical processes governing jet production appear to be universal, with characteristic length and time scales proportional to the black hole mass [Mirabel and Rodríguez, 1999]. This section provides an overview of the observational properties of astrophysical jets and discusses the two principal theoretical mechanisms proposed for their launching.

1.3.1 Observational properties of astrophysical jets

Astrophysical jets are identified primarily by their synchrotron emission, which is generated by relativistic electrons spiralling along magnetic fields. This non-thermal radiation is mainly detected at radio and infrared wavelengths and is characterised by a power-law spectrum $S_\nu \propto \nu^\alpha$, typically with a spectral index of $\alpha \approx -0.7$. Additional diagnostic features include high brightness temperatures, rapid variability, and linear polarisation [Mirabel and Rodríguez, 1999]. These characteristics are inconsistent with thermal emission processes and serve as a direct signature of non-thermal particle acceleration occurring within the jet structure.

Observations of X-ray binaries containing stellar-mass black holes have confirmed that jets in these systems propagate at relativistic bulk velocities. In the source GRS 1915 + 105, the simultaneous detection of bipolar radio ejecta moving in opposite directions allowed a direct measurement of the velocity of the jet. The approaching component displayed an apparent transverse velocity of $1.25c$. This phenomenon, known as superluminal motion, arises from light-travel-time effects when a source moves at a significant fraction of the speed of light towards the observer. For GRS 1915+105, the inferred intrinsic velocity is $v_{\mathrm{int}} = 0.92c$ at an inclination of $\theta = 70°$ to the line of sight [Mirabel and Rodríguez, 1999]. Similar relativistic motion has been observed in other sources, such as GRO J1655-40, indicating that such high-velocity outflows are a characteristic feature of black hole X-ray binaries.

1.3.2 Jet launching mechanisms

Two mechanisms have been proposed to explain the launching of relativistic jets from accreting black holes. Although both models rely on large-scale magnetic fields threading the system, they differ in their energy sources.

The first mechanism, developed by Blandford and Payne [1982], proposes that a magnetised Keplerian disc can drive a centrifugally accelerated outflow along magnetic field lines anchored in the disc surface. In the ideal magnetohydrodynamics (MHD) limit, these field lines are frozen into the conducting plasma and corotate with the disc. This frozen-in condition relates the fluid velocity $\vec{v}$ to the local magnetic field $\vec{B}$ in general coordinates' vectors through

$$\vec{v} = \frac{k}{4\pi\rho}\vec{B} + (\vec{\omega} \times \vec{r}), \tag{1.10}$$

where $k/4\pi$ is the ratio of the mass flux to the magnetic flux along a given field line (k may then be regarded as a key conserved quantity representing the mass loading along a magnetic field line), ρ is the gas density, and $\vec{\omega}$ is the angular velocity of the field line foot-point at the disc surface [Blandford and Payne, 1982]. Since $\vec{\omega}$ is constant along each field line, the plasma loaded into the field lines is forced to corotate with the disc.

The geometry of the poloidal field component governs whether the plasma is launched from the disc surface. This can be understood by considering the effective potential ϕ that combines gravity and centrifugal force experienced by a fluid element. Given that the element is initially at rest on a corotating field line, the potential ϕ in any point can be written as

$$\phi(R, z) = -\frac{GM_\bullet}{R_0}\left[\frac{1}{2}\left(\frac{R}{R_0}\right)^2 + \frac{R_0}{(R^2 + z^2)^{1/2}}\right] = \text{const.}, \tag{1.11}$$

where R_0 is the foot-point radius at the disc midplane. When the poloidal component of the magnetic field has an angle of less than 60° with the disc plane, the effective potential decreases outward along the field line, and the plasma is centrifugally accelerated away from the disc surface [Blandford and Payne, 1982]. Field lines inclined more steeply than this critical angle keep the plasma in stable equilibrium and do not produce an outflow. At large distances from the disc, the rotation of the field line foot-points gradually winds up the field into a predominantly toroidal configuration. The magnetic tension of this field acts as an inward hoop stress directed toward the rotation axis, collimating the outflow into a jet.

An alternative mechanism, focused on the extraction of rotational energy from the black hole, was formulated by Blandford and Znajek [1977]. In this model, a rotating black hole is threaded by an ordered poloidal magnetic field, which is supported by currents within the equatorial accretion disc. This configuration establishes a force-free magnetosphere surrounding the event horizon of the black hole. An outward Poynting flux is generated along the field lines crossing the event horizon, extracting the black hole's rotational energy electromagnetically. The resulting power depends on the angular velocity of the field lines relative to that of the event horizon [Blandford and Znajek, 1977]. This mechanism requires a rotating (Kerr) black hole and vanishes in the non-rotating Schwarzschild limit.

1.4 Astrophysical context

Accreting black holes are observed in two principal classes of astrophysical systems, differing primarily in the mass of the central object. These range from stellar-mass objects in Galactic X-ray binaries to supermassive black holes at the centres of distant active galaxies, spanning many orders of magnitude in both mass and luminosity. Despite the differences in characteristic scales, the same theoretical framework underlies the accretion physics in both regimes. Both classes of systems are therefore important for testing and developing accretion disc theory.

1.4.1 Stellar-mass black holes in X-ray binaries

Stellar-mass black holes are identified as X-ray binary systems where a black hole accretes material from a companion donor star. Depending on the mass of the companion, these systems are classified as either high-mass XRB (HMXBs) or low-mass XRB (LMXBs). In HMXBs, the donor is typically an early-type OB star, and mass transfer proceeds primarily via a stellar wind. In contrast, LMXBs involve a late-type, low-mass star transferring matter through Roche lobe overflow, a process that inevitably leads to the formation of an accretion disc [Frank et al., 2002]. Estimated masses for the black hole components in these systems typically range from approximately 3 to 20 $M_\odot$ [Remillard and McClintock, 2006].

The accretion process releases gravitational potential energy predominantly as X-ray radiation originating from the hot inner regions of the disc. This high-energy emission makes X-ray binaries one of the brightest sources in the sky, positioning them as critical observational laboratories for studying accretion physics and the effects of strong gravity near the black hole [Frank et al., 2002, Remillard and McClintock, 2006]. A notable subset of these systems, referred to as microquasars, launch relativistic jets and exhibit apparent superluminal motion, mirroring the behaviour of extragalactic radio sources [Mirabel and Rodríguez, 1999]. The observed disc-jet connection in microquasars suggests that the fundamental jet-launching mechanisms discussed in Section 1.3 operate across many orders of magnitude in black hole mass [Mirabel and Rodríguez, 1999].

1.4.2 Supermassive black holes in active galactic nuclei

Supermassive black holes (SMBHs) are thought to reside at the centres of most massive galaxies [Frank et al., 2002]. These objects, with masses ranging from 10^6 to 10^{10} $M_\odot$, power AGN, which are among the most luminous persistent sources in the observable Universe, with bolometric luminosities reaching up to 10^{47} erg s^{-1} [Frank et al., 2002]. AGN appear in a variety of observational forms, including Seyfert galaxies and quasars, but the underlying energy source in each case is gravitational energy released by accretion onto the central black hole [Frank et al., 2002]. A prominent example is Sagittarius A* (Sgr A*), the compact radio source at the centre of our own Galaxy, with a mass of 4.15×10^6 $M_\odot$ [Gravity Collaboration et al., 2019].

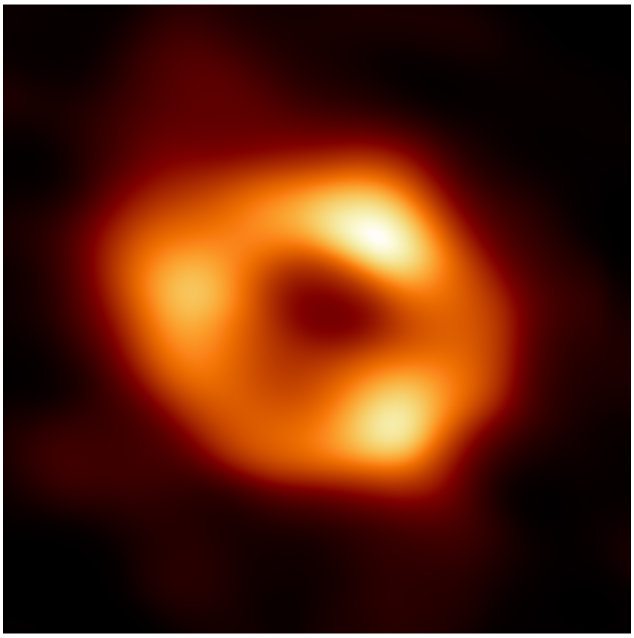

Figure 1.1: First image of Sgr A*, the supermassive black hole at the centre of the Milky Way, obtained at 1.3 mm wavelength by the Event Horizon Telescope [Event Horizon Telescope Collaboration et al., 2022]. The bright emission ring surrounds a dark central shadow cast by the black hole.

The physics governing accretion in AGN is fundamentally the same as in XRB, differing primarily in the characteristic mass and spatial scales involved. This universality is further supported by the observation that many AGN drive powerful relativistic jets. These outflows can extend from kiloparsec to megaparsec scales and exhibit superluminal motion of compact components, providing a direct extragalactic analogy to the microquasars observed on stellar scales [Mirabel and Rodríguez, 1999]. As discussed in Section 1.3, the same jet-launching mechanisms are believed to operate in both classes of system, reinforcing the physical connection between stellar-mass and SMBH.

Chapter 2

Gas dynamics and disc structure

All accreting matter is in a gaseous form, which means that, rather than interacting by short-range forces, the accreting particles directly affect one another by collisions. The distance a particle travels on average between collisions is called the mean free path l. On the length scales $L \gg l$, we can assume that the gas is a continuous fluid described by a velocity $\vec{V}$, temperature T, and density ρ at each point. Implementing the laws of conservation of mass, momentum, and energy lets us study the behaviour of fluid variables as functions of time t and position $\vec{r}$.

2.1 Continuity equation

The continuity equation expresses the conservation of mass for the fluid [Frank et al., 2002],

$$\frac{\partial \rho}{\partial t} + \vec{\nabla} \cdot (\rho \vec{V}) = 0. \tag{2.1}$$

In a cylindrical coordinate system (R, ϕ, z), assuming axial symmetry and a geometrically thin disc, the continuity equation takes the form

$$R \frac{\partial \Sigma}{\partial t} + \frac{\partial}{\partial R} (R \Sigma V_R) = 0, \tag{2.2}$$

where Σ is the surface density, defined as the vertical integral of the volume density,

$$\Sigma = \int_{-\infty}^{\infty} \rho \, \mathrm{d}z. \tag{2.3}$$

2.2 Equation of state

Due to the thermal motion of the particles, the gas can be characterised at each point by a pressure P. For a non-degenerate gas, the relation between pressure, density, and temperature is given by the ideal gas equation of state [Frank et al., 2002],

$$P = \frac{k \rho T}{\mu m_u}, \tag{2.4}$$

where k is the Boltzmann constant, m_u is the unit of atomic mass , and μ is the mean molecular weight, which gives a measure of the chemical composition and ionisation state of the gas. For example, $\mu = 1$ for neutral hydrogen and $\mu = 1/2$ for fully ionised hydrogen.

Due to the dependence of gas pressure on both local density and temperature, it is advantageous to introduce the isothermal sound speed, a, defined as

$$a^2 = \frac{P}{\rho} = \frac{kT}{\mu m_u}, \tag{2.5}$$

which facilitates a more compact representation of the equation of state in the form $P = a^2\rho$. Physically, the speed of sound a governs the velocity with which small pressure perturbations propagate through the medium under isothermal conditions. Within the framework of the thin disc approximation, this quantity serves as a fundamental thermal velocity scale, providing a critical benchmark against which the azimuthal orbital velocity, V_ϕ, is evaluated. This comparison is essential for determining the Mach number of the flow and consequently the vertical structure and stability of the accretion disc.

2.2.1 Euler equation and momentum conservation

Pressure gradients within the gas give rise to net forces on each fluid element, as they result in a transfer of momentum across the gas. All other forces acting on the gas are encapsulated in the force density $\vec{f}$. Conservation of momentum for each gas element gives the Euler equation, also known as the equation of motion [Frank et al., 2002],

$$\rho \left(\frac{\partial \vec{V}}{\partial t} + (\vec{V} \cdot \vec{\nabla})\vec{V} \right) = -\vec{\nabla} P + \vec{f}. \tag{2.6}$$

In cylindrical coordinates with the thin disc approximation, the radial momentum conservation equation becomes [Kurfürst et al., 2014]

$$\frac{\partial V_R}{\partial t} + V_R \frac{\partial V_R}{\partial R} = \frac{V_\phi^2}{R} - \frac{GM_\bullet}{R^2} - \frac{1}{\Sigma}\frac{\partial (a^2\Sigma)}{\partial R} + \frac{3}{2}\frac{a^2}{R}, \tag{2.7}$$

where $M_\bullet$ is the mass of the central object. The right-hand side of equation (2.7) contains four distinct contributions. The first term, V_ϕ^2/R, is the centrifugal acceleration arising from the azimuthal motion of the gas. The second term, $-GM/R^2$, is the radial gravitational acceleration directed towards the central object. The third term, $-(1/\Sigma)\,\partial(a^2\Sigma)/\partial R$, represents the force of the pressure gradient per unit mass, which accounts for the thermal pressure support in the disc. The last term, $(3/2)\,a^2/R$, originates from the expression for gravitational acceleration in cylindrical coordinates evaluated within the thin disc approximation, where the disc thickness is negligible with respect to the radial distance of any point studied.

Requiring azimuthal momentum to be conserved gives [Kurfürst et al., 2014]

$$\frac{\partial V_\phi}{\partial t} + V_R \frac{\partial V_\phi}{\partial R} + \frac{V_R V_\phi}{R} = f_{\text{visc}}, \tag{2.8}$$

where f_{visc} is the viscous force per unit volume, representing the net azimuthal friction force acting on a fluid element due to the differential rotation between neighbouring disc rings.

2.3 Energy equation

The principle of energy conservation for a compressible viscous fluid requires a formulation that integrates the evolution of both the kinetic and thermal components. We define the total energy density E as the sum of the kinetic and specific internal energy densities [Mihalas and Mihalas, 1984],

$$E = \frac{1}{2}\rho V^2 + \rho\varepsilon, \tag{2.9}$$

where ε represents the specific internal energy, and the velocity magnitude is given by $V^2 = V_R^2 + V_\phi^2 + V_z^2$ in cylindrical coordinates.

To derive the evolution of kinetic energy, we take the dot product of the velocity vector $\vec{V}$ with the momentum equation, yielding

$$\rho\frac{D}{Dt}\left(\frac{1}{2}V^2\right) = \vec{\nabla}\cdot\left(\vec{V}\cdot\mathbf{T}\right) + P\,\vec{\nabla}\cdot\vec{V} - \Psi. \tag{2.10}$$

Here, $\mathbf{T}$ denotes the Cauchy stress tensor defined in Section A.4, and $\Psi = \sigma_{ij}\,\partial V_i/\partial x_j$ is the viscous dissipation function, which accounts for the irreversible transformation of the bulk kinetic motion into microscopic thermal energy. Similarly, the internal energy evolves in accordance with the first law of thermodynamics.

$$\rho\frac{D\varepsilon}{Dt} = -P\,\vec{\nabla}\cdot\vec{V} + \Psi - \vec{\nabla}\cdot\vec{q}, \tag{2.11}$$

where $\vec{q}$ is the heat flux vector. The term $-P\,\vec{\nabla}\cdot\vec{V}$ describes energy changes due to compression or expansion, while Ψ provides the heating rate due to viscous dissipation.

By combining equations (2.10) and (2.11), the terms representing $P\,\mathrm{d}V$ work and viscous dissipation cancel, highlighting the conservative exchange between the two energy forms. Transforming the result into a conservative Eulerian framework via the continuity equation leads to the total energy equation,

$$\frac{\partial E}{\partial t} + \vec{\nabla}\cdot\left[(E+P)\,\vec{V}\right] = \vec{\nabla}\cdot\left(\vec{V}\cdot\boldsymbol{\sigma} - \vec{q}\right), \tag{2.12}$$

where $\boldsymbol{\sigma}$ is the viscous stress tensor from equation (A.20). Equation (2.12) is the form implemented within the *CASTRO* code. The left-hand side represents the local rate of change of total energy and its advection through the enthalpy flux $(E+P)\vec{V}$, while the right-hand side encapsulates the work performed by viscous stresses and losses or gains via thermal conduction.

Solving the full energy equation self-consistently remains a significant numerical challenge, primarily because it requires an exact treatment of the radiative cooling function and the varying opacity within the disc. Consequently, the simulations in this work employ an isothermal approximation, in which the temperature is not solved dynamically but is instead prescribed by a radial power-law profile [Kurfürst et al., 2014],

$$T(R) = T_0 \left(\frac{R_{\rm eq}}{R} \right)^p , \tag{2.13}$$

where T_0 is the temperature at the inner disc reference radius $R_{\rm eq}$ and $p \geq 0$ is a dimensionless parameter that determines the radial temperature gradient. Under this approximation, equation (2.12) is not solved and the disc's thermal structure is held fixed. This simplification is standard practice in thin disc modelling, where the primary dynamical features are governed by the momentum balance and the transition between the subsonic and supersonic flow regimes rather than by the local energy budget [Kurfürst et al., 2014].

2.4 Vertical Disc Structure and Hydrostatic Equilibrium

While the radial evolution of the disc is governed by the conservation laws derived in the preceding sections, its vertical extent is determined by the competition between the vertical pressure gradient and the vertical component of the gravitational force. Under the thin disc approximation, we assume that the fluid remains in a state of hydrostatic equilibrium along the z-axis [Kurfürst, 2015]. This implies that vertical accelerations are negligible compared to the primary forces, leading to the equilibrium condition:

$$\frac{\partial P}{\partial z} = -\rho g_z, \tag{2.14}$$

where g_z represents the vertical component of the gravitational acceleration. Assuming a point-mass gravitational potential $\Phi(R, z)$ as defined in eq.(A.15), the corresponding vertical acceleration is expressed as

$$g_z = -\frac{\partial \Phi}{\partial z} = -\frac{GM_\bullet z}{(R^2 + z^2)^{3/2}}. \tag{2.15}$$

In the limit of a thin disc, where the height z is significantly smaller than the radial distance R ($z \ll R$), the expression for g_z simplifies to

$$g_z \approx -\frac{GM_\bullet}{R^3} z = -\Omega_K^2 z, \tag{2.16}$$

where $\Omega_K = \sqrt{GM/R^3}$ denotes the Keplerian angular velocity. Substituting this linear approximation into (2.14) and employing the isothermal equation of state, $P = a^2\rho$, we obtain a differential equation for the vertical density distribution:

$$\frac{\partial \rho}{\partial z} = -\frac{\Omega_K^2}{a^2} \rho \, z. \tag{2.17}$$

This relation represents a separable first-order ordinary differential equation. Integration with respect to z yields a Gaussian density profile:

$$\rho(R, z) = \rho_0(R) \exp\left(-\frac{z^2}{2H^2}\right), \tag{2.18}$$

where $\rho_0(R)$ is the density in the disc mid-plane ($z = 0$), and H is the vertical scale height, defined as

$$H = \frac{a}{\Omega_K} = a\sqrt{\frac{R^3}{GM_\bullet}}. \tag{2.19}$$

The scale height H serves as the characteristic measure of the disc's vertical thickness at a given radius. The total surface density, Σ, is subsequently recovered by integrating the density profile over the entire vertical range:

$$\Sigma(R) = \int_{-\infty}^{\infty} \rho(R, z)\, \mathrm{d}z = \sqrt{2\pi}\, H\, \rho_0(R). \tag{2.20}$$

The validity of the thin disc approximation rests on the requirement that $H \ll R$ [Frank et al., 2002], which, according to equation (2.19), is equivalent to the condition that the azimuthal motion is highly supersonic ($V_\phi \gg a$). This criterion is typically satisfied in the inner regions of the accretion discs, where the deep gravitational potential maintains high orbital velocities relative to the local thermal energy. Furthermore, the scale height is intrinsically linked to the transport of angular momentum; in the Shakura-Sunyaev prescription, the kinematic viscosity is parametrised as $\nu \approx \alpha a H$ [Kurfürst et al., 2014, Shakura and Sunyaev, 1973]. This coupling demonstrates that the vertical stratification and radial dynamics of the disc are not isolated phenomena but are fundamentally interconnected through the mechanism of turbulent viscosity.

2.5 Viscosity and the Shakura-Sunyaev prescription

In the axisymmetric ($\partial/\partial\phi = 0$) and geometrically thin case, the viscous force density is given by [Kurfürst et al., 2014]

$$f_{\mathrm{visc}} = \frac{\partial T_{R\phi}}{\partial R} + \frac{2T_{R\phi}}{R}, \tag{2.21}$$

where $T_{R\phi}$ denotes the R-ϕ component of the viscous stress tensor, which describes the tangential stress between the adjacent radial layers of the disc. Taking into account the turbulent motion of the gas, the kinematic viscosity ν can be written as

$$\nu = \alpha\frac{a^2 R}{V_\phi} \approx \alpha a H, \tag{2.22}$$

where α is the dimensionless Shakura-Sunyaev parameter [Shakura and Sunyaev, 1973] and H is the vertical scale height of the disc.

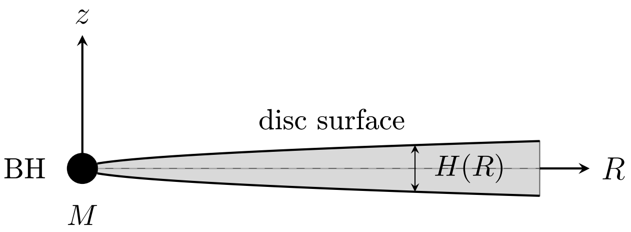

Figure 2.1: Schematic cross-section of a geometrically thin accretion disc in cylindrical coordinates $(R,\, z)$. The vertical scale height $H(R)$, defined by equation (2.19), characterises the local disc thickness at each radius. The filled circle represents the central compact object of mass $M_\bullet$.

The viscous force density $f_{\rm visc}$ is usually represented using the first-order linear viscosity term,

$$f^{(1)}_{\rm visc} = -\frac{1}{R^2\Sigma}\frac{\partial}{\partial R}\left(\alpha a^2 R^2 \Sigma\right). \tag{2.23}$$

Including the full second-order Navier-Stokes viscosity term, the right-hand side of equation (2.8) takes the form of

$$f^{(2)}_{\rm visc} = \frac{1}{R^2\Sigma}\frac{\partial}{\partial R}\left(\alpha a^2 R^3 \Sigma \frac{\partial \ln V_\phi}{\partial R} - \alpha a^2 R^2 \Sigma\right). \tag{2.24}$$

The radial profile of α is generally not constant throughout the disc. We therefore adopt the power-law parametrisation

$$\alpha = \alpha_0 \left(\frac{R_{\rm eq}}{R}\right)^n, \tag{2.25}$$

where α_0 is the value of α at the inner disc boundary and $n \geq 0$ is a free parameter that describes the radial dependence of viscosity. An equivalent result is recovered from the angular momentum conservation equation [Pringle, 1981, Frank et al., 2002],

$$\frac{\partial}{\partial t}\left(\Sigma R^2 \Omega\right) + \frac{1}{R}\frac{\partial}{\partial R}\left(\Sigma V_R R^3 \Omega\right) = \frac{1}{2\pi R}\frac{\partial G}{\partial R}, \tag{2.26}$$

where $\Omega = V_\phi / R$ is the angular velocity and G is the viscous torque acting between two neighbouring disc segments,

$$G = 2\pi \alpha a^2 \Sigma R^3 \frac{\partial \ln \Omega}{\partial R}. \tag{2.27}$$

2.6 Stationary Thin disc Approximation

The comprehensive time-dependent equations derived in the previous sections can be significantly simplified by adopting the stationary thin disc approximation. This framework is defined by the simultaneous imposition of three physical constraints: the disc is assumed to be in a steady state ($\partial/\partial t = 0$), it is geometrically thin and vertically integrated ($\partial/\partial z = 0$), and it possesses axial symmetry ($\partial/\partial\phi = 0$). Under these assumptions, the fluid properties are reduced to functions of the radial coordinate R only [Kurfürst, 2015].

Applying the condition of stationarity to the continuity equation leads to:

$$\frac{\partial}{\partial R}\left(R\Sigma V_R\right) = 0, \tag{2.28}$$

implying that the product $R\Sigma V_R$ remains spatially invariant across the disc. This constant is physically identified with the mass accretion rate, $\dot{M}_\bullet$, representing the mass flux through a cylindrical surface per unit time:

$$\dot{M}_\bullet = -2\pi R\Sigma V_R = \text{const.} \tag{2.29}$$

According to standard convention, the negative sign ensures that $\dot{M} > 0$ for an inward radial flow ($V_R < 0$). The accretion rate is a fundamental parameter that determines the overall energetic output and luminosity of the system.

In the stationary limit, the radial momentum equation simplifies to a balance between gravitational pull, centrifugal acceleration, and the radial pressure gradient. For a cold disc, where thermal pressure support is negligible compared to the rotational velocity ($a \ll V_\phi$), the momentum balance is dominated by the centrifugal and gravitational terms:

$$\frac{V_\phi^2}{R} \approx \frac{GM_\bullet}{R^2}. \tag{2.30}$$

This equilibrium results in an azimuthal velocity profile that is approximately Keplerian, $V_\phi \approx V_K$, consistent with equation (A.17). Small deviations from this profile occur only due to the residual effects of viscous stresses and minor pressure gradients.

Combining equation (2.28) with the angular momentum equation and imposing the condition that the viscous torque vanishes at the outer boundary R_out, the radial drift velocity of a stationary Keplerian disc can be related to the kinematic viscosity [Kurfürst, 2015]:

$$V_R \approx -\frac{3\alpha a H}{2R}\left[\sqrt{\frac{R_\text{out}}{R}} - 1\right]^{-1}, \tag{2.31}$$

where R_out denotes the radius at which the viscous torque vanishes. Equation (2.31) illustrates that the radial inward drift is significantly slower than both the local sound speed and the orbital velocity. This hierarchy of velocities ($|V_R| \ll a \ll V_\phi$) confirms the self-consistency of the thin disc model. Consequently, the disc material spirals inward on the viscous timescale, $t_\text{visc} \sim R^2/\nu$. Given that this timescale is typically several orders of magnitude greater than the orbital period $t_\text{orb} = 2\pi/\Omega_K$, the disc can be treated as a quasi-stationary structure over many orbital revolutions.

Chapter 3

Numerical methods

3.1 The CASTRO code

The numerical simulations discussed in this thesis were carried out with *CASTRO*, an open-source solver for compressible astrophysical hydrodynamics originally developed at Lawrence Berkeley National Laboratory and currently maintained within the *AMReX-Astrophysics* collaboration [Almgren et al., 2010]. The code was adopted mainly because it provides a native implementation of the compressible hydrodynamic equations in cylindrical coordinates and combines this formulation with adaptive mesh refinement (AMR), which is advantageous for accretion-disc problems where both the geometry and the relevant spatial scales span a wide dynamic range. The *AMReX* software framework underpinning *CASTRO*, together with the specific setup employed in the present work, is outlined in the following subsections.

3.1.1 General description and capabilities

CASTRO flows on a fixed Eulerian mesh, with support for adaptive mesh refinement [Almgren et al., 2010]. The code is written in a combination of C++ and Fortran90 and is designed for large-scale parallel simulations. Parallelisation is achieved using MPI for communication between computing nodes and OpenMP for shared-memory parallelism within a node, and the code can also run on GPU-based systems [Katz et al., 2020]. Simulations can be run in one, two, or three spatial dimensions, and the code supports Cartesian, cylindrical, and spherical coordinate systems [Almgren et al., 2010].

Beyond pure hydrodynamics, *CASTRO* includes optional modules for self-gravitation, nuclear reaction networks, and radiation hydrodynamics, depending on the physical problem being studied [Almgren et al., 2010]. In this thesis, we focus on the hydrodynamic and gravitational structure of the accretion flow; therefore, a gamma-law equation of state is employed, while nuclear reaction networks are not activated. This simplifies the model and focuses on the dynamics of the disc.

The hydrodynamic equations are integrated using an unsplit implementation of the piecewise parabolic method (PPM), which is described in detail in Section 3.1.3. *CASTRO* further supports temporal sub-cycling, i.e. the use of smaller time steps on refined AMR levels than on coarser levels, and the refinement does not require a fixed relationship between coarser and finer grid patches [Almgren et al., 2010].

The simulation data are written using the *AMReX* plotfile format. This output is organised as a directory structure that contains all data from the AMR grid at each output time and is compatible with standard post-processing and visualisation tools, including `yt` and `VisIt` [Almgren et al., 2010].

3.1.2 The AMReX framework and adaptive mesh refinement

CASTRO is built on *AMReX*, an open-source software framework for block-structured adaptive mesh refinement applications [Zhang et al., 2019]. *AMReX* provides the underlying data structures, parallel communication routines, and grid management routines on which *CASTRO* physics solvers operate and is designed to run efficiently on both CPU- and GPU-based architectures.

The AMR methodology implemented in *AMReX* organises the computational domain as a nested hierarchy of logically rectangular grids, ranging from a coarsest base level to a finest level determined at runtime. Each level consists of a union of non-overlapping rectangular patches of a given resolution, and finer levels are properly nested within coarser ones, meaning that every fine-level patch is fully contained within the union of patches at the level immediately below it. The refinement ratio between adjacent levels is typically a factor of two or four, applied uniformly in all coordinate directions [Almgren et al., 2010].

The grid hierarchy is not fixed for the entire simulation. Instead, it is updated regularly based on criteria specified by the user, such as large gradients in density or pressure. Cells that meet these criteria are marked for refinement and grouped into new rectangular patches at the next level using a dedicated clustering algorithm [Berger and Rigoutsos, 1991]. Cells that no longer meet the criteria are returned to the lower-resolution grid.

Each level of the grid hierarchy is advanced in time using a time step appropriate to its own resolution. Because finer grids have smaller cells, they require smaller time steps to remain numerically stable. A fine level, therefore, takes several steps for every single step of the coarser level beneath it. Once the fine level has caught up in time with the coarse level, the two solutions are merged: the fine level data are averaged onto the coarse grid, and any small conservation errors that arise at the boundary between the two levels are corrected [Almgren et al., 2010].

In the context of accretion disc simulations, AMR is particularly valuable because the physical processes of interest are concentrated near the central object, where density gradients are steep and high spatial resolution is required, while the outer disc regions can be represented at coarser resolution without significant loss of accuracy.

3.1.3 Hydrodynamic solver

CASTRO solves the fully compressible equations of hydrodynamics in conservation form, as described by Almgren et al. [2010]. The three governing equations express the conservation of mass, momentum, and total energy:

$$\frac{\partial \rho}{\partial t} = -\nabla \cdot (\rho \mathbf{u}) + S_{\mathrm{ext},\rho}, \tag{3.1}$$

$$\frac{\partial (\rho \mathbf{u})}{\partial t} = -\nabla \cdot (\rho \mathbf{u}\mathbf{u}) - \nabla p + \rho \mathbf{g} + \mathbf{S}_{\mathrm{ext},\rho\mathbf{u}}, \tag{3.2}$$

$$\frac{\partial (\rho E)}{\partial t} = -\nabla \cdot (\rho \mathbf{u} E + p\mathbf{u}) + \rho \mathbf{u} \cdot \mathbf{g} + \rho H_{\mathrm{nuc}} + S_{\mathrm{ext},\rho E}. \tag{3.3}$$

Here ρ is the mass density, $\mathbf{u}$ is the velocity vector, p is the thermal pressure, $\mathbf{g}$ is the gravitational acceleration vector, and $E = e + |\mathbf{u}|^2/2$ is the total energy per unit mass, which is the sum of the specific internal energy e and the specific kinetic energy. The pressure does not evolve directly but is derived from the conserved variables through the gamma-law equation of state introduced in Section 2.2. The terms S_{ext} denote the terms specified by the user of external sources , and H_{nuc} is the rate of nuclear energy generation.

In the simulations presented in the thesis, several of these source terms are inactive. Nuclear reaction networks are not employed, so $H_{\mathrm{nuc}} = 0$ and the mass fraction equations are not evolved. Radiation hydrodynamics is likewise disabled, and all external source terms are set to zero. The only active source is the gravitational acceleration $\mathbf{g}$ arising from the central point mass, which enters both the momentum and energy equations and is described in Section 3.1.4. The system, therefore, reduces to the compressible Euler equations with a gravitational source term.

These equations are discretised using the piecewise parabolic method (PPM) of Colella and Woodward [1984], a finite-volume scheme in which a parabolic profile is reconstructed within each grid cell at every time step. The reconstructed states at cell interfaces are used to compute the fluxes that advance the conserved variables forward in time. The complete multi-dimensional update is performed in a single unsplit step following Miller and Colella [2002], and the time step is controlled by the Courant–Friedrichs–Lewy (CFL) stability condition with a CFL number of 2/3.

3.1.4 Gravitation implementation

In *CASTRO*, gravitation is added as a source term in the momentum and energy equations described in Section 3.1.3. The gravitational acceleration vector, defined as $\mathbf{g} = -\nabla\Phi$, connects the gravitational potential Φ directly to the hydrodynamic evolution. There are three options for computing this potential: a constant gravitational acceleration, a monopole approximation, or a full solution of the Poisson equation [Almgren et al., 2010]. The gravitation type is chosen at runtime in the inputs file, which makes it easy to select the level of approximation that fits the physical problem being studied.

Beyond these standard solvers, *CASTRO* also supports adding a point mass contribution to the gravitational potential. Because the Poisson equation is linear, the gravitational acceleration from the point mass is simply added on top of the acceleration from the main gravitational solver. This means that the point mass option works with all three gravitational types. The code also allows the density in the grid cells immediately around the point mass to be kept constant at each time step, so that any mass moving into those cells from the surrounding fluid is transferred to the point mass instead of building up on the grid. This gives a simple numerical model for mass accretion onto a compact central object.

The gravitational energy source term can be handled in several ways. The most accurate option evaluates the energy change at cell faces using the hydrodynamic mass fluxes rather than at cell centres. This conservative approach is important for keeping the total energy preserved throughout the simulation, which is especially important for long-duration accretion disc calculations [Almgren et al., 2010].

As discussed in Section A.3, the standard Newtonian point-mass potential does not reproduce relativistic features such as the innermost stable circular orbit. The Paczyński–Wiita pseudo-Newtonian potential would be a better approximation near the black hole, but it is not used in the current *CASTRO* setup. This is a known limitation of the current simulations and is discussed further in Chapter 6.

3.2 SEDONA

The *CASTRO* simulations described in the preceding section were performed with the radiation module disabled, meaning that the code solves only the hydrodynamic and magnetohydrodynamic equations without coupling to the radiation field. As a consequence, the emergent spectra of the accretion flow cannot be obtained directly from the simulation output and must instead be computed in a separate post-processing step.

For this purpose, we employ *SEDONA*, a multi-dimensional Monte Carlo radiative transfer code developed by Kasen et al. [2006]. In the Monte Carlo approach adopted by *SEDONA*, the radiation field is discretised into a large number of monochromatic energy packets, each representing a collection of photons at a given frequency [Kasen et al., 2006]. These packets are emitted from within the gas and propagated through the computational domain, where they undergo scattering and absorption events; the probability of each interaction is determined by the local opacity at the packet's current position. The ionisation and excitation states of the gas are treated under the assumption of local thermodynamic equilibrium (LTE) [Kasen et al., 2006]. Once the packets escape the domain, the emergent spectrum is assembled as a function of both frequency and viewing angle, with $\mu = \cos\theta$, where θ is the polar angle measured from the rotation axis.

Although *SEDONA* was originally developed for the study of supernova atmospheres, the underlying Monte Carlo radiative transfer method is general enough to be applied to other astrophysical configurations. The spatial grid supports one-dimensional spherical, two-dimensional cylindrical, and three-dimensional Cartesian geometries [Kasen et al., 2006], the last of which is fully consistent with the *CASTRO* MHD setup described in Chapter 4. The iterative convergence scheme employed by SEDONA cycles through successive estimates of the temperature structure and opacity until the radiation field reaches a state of radiative equilibrium, defined as the point at which the rate of photon absorption equals the rate of thermal emission at every point in the domain [Kasen et al., 2006]. The convergence of the Monte

Carlo method has been shown to be rapid and stable, even for complicated multi-dimensional configurations [Kasen et al., 2006].

In the present work, the input model for *SEDONA* was constructed directly from the three-dimensional MHD *CASTRO* output files. Specifically, the spatial distributions of density, temperature, and the three components of the velocity field were extracted and converted to the *SEDONA* input format. The code was then run iteratively until the radiation field converged to a state of radiative equilibrium, as described above. Separate radiative transfer calculations were performed for each magnetic field configuration considered in the simulations. The resulting spectra were subsequently post-processed to extract the wavelength-dependent flux for selected viewing angles and to compute both the bolometric luminosity and the bolometric magnitude as functions of viewing angle. The specific spectral resolution and the number of viewing angles adopted in the calculations are described in Chapter 4.

Chapter 4

Simulation setup

In this thesis, two simulations are used to study accretion dynamics and jet formation. A two-dimensional hydrodynamic simulation, performed in cylindrical coordinates, serves as the fundamental model of the accretion disc. The second simulation adds a magnetic field to examine how it affects the disc structure and the jets that are already developing in the hydrodynamic simulation. While the former uses cylindrical symmetry, the latter is implemented in a Cartesian coordinate system. This is required due to a limitation of *CASTRO*, as its MHD solver is not available for cylindrical grids [Almgren et al., 2010]. To allow for a direct comparison between the purely hydrodynamic and magnetohydrodynamic regimes, both simulations use the same physical parameters, including the domain dimensions, the central black hole mass, the equation of state, and the total integration time. Another limitation stems from the fact that *CASTRO* does not allow for the inclusion of general relativistic effects; for this reason, the maximum possible speed in our models was somewhat artificially limited to $0.9c$ in order to avoid potentially non-physical evolution. It should be noted, however, that only a few local cases of a possible violation of this speed limit appeared in the simulation.

4.1 2D cylindrical hydrodynamic simulation

The two-dimensional simulation models the accretion disc in cylindrical coordinates $(R,\, z)$, exploiting the axial symmetry of the system. The computational domain extends from $R \in [0,\, 1.8 \times 10^{15}]$ cm in the radial direction and $z \in [-1.8 \times 10^{15},\, +1.8 \times 10^{15}]$ cm in the vertical direction, which corresponds to a physical scale of approximately 1.2×10^{2} au in each dimension. The domain is discretised on a uniform grid of 2400×4800 cells, yielding a constant cell size of $\Delta x = 7.5 \times 10^{11}$ cm. Adaptive mesh refinement is deactivated for this setup, consequently, the spatial resolution remains uniform throughout the domain and across the entire integration period. On the symmetry axis ($R = 0$), a reflecting boundary condition is imposed, enforcing a zero normal velocity and a zero normal gradient for all other physical quantities. Outflow boundary conditions are applied to all remaining boundaries, allowing material to exit the domain freely without numerical reflections.

The central black hole is treated as a point mass of $M_\bullet = 4 \times 10^{6}\, M_\odot$ situated at the origin. Mass accretion is modelled by removing fluid that enters the innermost grid cells and adding it to the central point mass. The gravitational potential is determined by solving the Poisson equation at each time step using the `PoissonGrav` solver provided by *CASTRO* [Almgren et al., 2010]. The remaining physics modules, including magnetohydrodynamics, radiation hydrodynamics, and nuclear reaction networks, are disabled. The gas is described by a gamma-law equation of state with an adiabatic index of $\gamma = 5/3$ and a mean molecular weight of $\mu = 0.62$, appropriate for a fully ionised plasma of solar composition.

The initial density distribution comprises two components. The disc component follows the vertical Gaussian profile established in Eq. (2.18), where the local scale height $H(R)$ is defined according to Eq. (2.19). The mid-plane density $\rho_0(R)$ is then normalised at the inner boundary radius $r_{BH} = 1.186 \times 10^{12}$ cm using the Eddington accretion rate $\dot{M}_{Edd}$.

An ambient medium component of the form

$$\rho_{\rm CSM}(r) = \frac{\rho_{\rm B}\, r_{\rm B}}{r}, \tag{4.1}$$

with $\rho_{\rm B} = 1.612 \times 10^{-23}\,{\rm g\,cm^{-3}}$ and $r_{\rm B} = 5.34 \times 10^{17}\,{\rm cm}$, is added to prevent the formation of numerical vacuum regions in the outer domain. The temperature is initialised with a power-law profile,

$$T(r) = T_0 \left(\frac{r_{\rm BH}}{r}\right)^{3/4}, \tag{4.2}$$

where T_0 is the effective temperature at $r_{\rm BH}$, determined from the standard thin-disc relation evaluated at the Eddington accretion rate [Shakura and Sunyaev, 1973]. The initial velocity field follows a Keplerian azimuthal profile,

$$V_\phi(R, z) = \sqrt{GM_\bullet}\, \frac{R}{(R^2 + z^2)^{3/4}}, \tag{4.3}$$

which reduces to $V_K = \sqrt{GM_\bullet/R}$ in the disc mid-plane, consistent with equation (A.17). The radial and vertical velocity components are set to zero at $t = 0\,{\rm d}$. The Shakura-Sunyaev viscosity parameter $\alpha = 0.1$ enters the initial conditions through its effect on the ratio between the azimuthal and radial velocity components at the disc base $r_{\rm BH}$, as prescribed in the problem initialisation routine. The viscosity parameter is taken to be spatially uniform throughout the domain. This corresponds to $n = 0$ in the power law parametrisation of equation (2.25). No explicit viscous source terms are added to the momentum equation during temporal evolution. Instead, the simulation solves the compressible Euler equations with a gravitational source term, where angular momentum transport arises from the numerical viscosity inherent to the PPM solver. This approach constitutes a known limitation of the current setup, and its implications for the interpretation of the results are addressed in Chapter 6.

Time integration is performed using the unsplit PPM scheme described in Section 3.1.3 [Almgren et al., 2010] with a CFL number of 2/3. To prevent superluminal velocities near the point mass, where Keplerian speeds under a Newtonian potential can approach a significant fraction of the speed of light, a velocity ceiling of $v_{\mathrm{lim}} = 2.4 \times 10^{10}\,\mathrm{cm\,s^{-1}} \approx 0.8c$ is enforced. A sponge layer is applied between $r = 3 \times 10^{12}$ cm and $r = 6.5 \times 10^{12}$ cm with a characteristic timescale of 10^4 s to suppress numerical oscillations near the inner boundary. The simulation was integrated until the hydrodynamic outflow reached the domain boundaries, indicating that the system had achieved a quasi-steady state. This occurred at $t \approx 5.4 \times 10^6$ s, corresponding to approximately 62 days, with plot files written every 10^4 s.

4.2 3D Cartesian MHD solution

The second set of simulations extends the model to three spatial dimensions and incorporates a magnetic field, with the aim of investigating how the field strength affects the disc structure and the character of the resulting outflow. Due to the limitations of the magnetohydrodynamic solver within the *CASTRO* framework regarding cylindrical coordinate systems, these simulations are conducted using a three-dimensional Cartesian grid. The computational domain encompasses $x, y, z \in [-1.8 \times 10^{15}, +1.8 \times 10^{15}]$ cm in all coordinate directions. This volume is discretised on a uniform grid of 360^3 cells, which yields a constant spatial resolution of $\Delta x = 10^{13}$ cm. Adaptive mesh refinement is not employed in this configuration. Outflow boundary conditions are applied to all six domain boundaries. The sponge layer used in the two-dimensional simulations is deactivated for this setup. The central black hole mass, the equation of state, the gravitational solver and the simulation stop time are identical to the parameters described in Section 4.1. This consistency ensures a reliable physical basis for the comparison between the hydrodynamic and magnetohydrodynamic approaches.

The magnetic field is initialised as a magnetic dipole aligned with the z-axis. By expanding the coordinate-free expression for a dipole field into Cartesian components [Griffiths, 2017], the three field components are defined as follows:

$$B_x = \frac{3m_1 xz}{r^5}, \quad B_y = \frac{3m_1 yz}{r^5}, \quad B_z = \frac{3m_1 z^2}{r^5} - \frac{m_1}{r^3}, \tag{4.4}$$

where $r = (x^2+y^2+z^2)^{1/2}$ represents the spherical radial distance and m_1 denotes the dipole moment parameter, given in units of $\mathrm{erg\,G^{-1}} = \mathrm{G\,cm^3}$. To prevent numerical instabilities at the origin, the magnetic field is set to zero within the black hole radius $r_{\mathrm{BH}} = 1.186 \times 10^{12}$ cm.

Three separate simulations are conducted with increasing field intensities, referred to throughout this thesis as the weak-field, mid-field, and strong-field configurations. These correspond to field strengths of 50 G, 100 G, and 200 G respectively, evaluated at the gravitational radius $r_{\mathrm{g}} = GM_\bullet/c^2$. The corresponding dipole moment parameters are $m_1 = 8.341 \times 10^{37}$, 1.668×10^{38}, and $3.336 \times 10^{38}\,\mathrm{erg\,G^{-1}}$ for the weak-field, mid-field, and strong-field cases, respectively. The weak-field and mid-field values fall within the range of ordered magnetic field strengths estimated from multi-wavelength observations of the inner accretion flow of Sgr A*, where typical values lie in the range of approximately 10–100 G [Michail et al., 2024]. The strong-field case at 200 G is included as an exploratory upper limit, as field strengths of this magnitude near the event horizon are not excluded by general relativistic MHD modelling [Ressler et al., 2020].

Chapter 5

Simulation results and analysis

5.1 2D Cylindrical hydrodynamic simulation

The initial configuration of the simulation, as illustrated in Figure 5.1, establishes a geometrically thin accretion disc residing within the mid-plane ($z = 0$). The density profile exhibits a steady decrease with increasing radial distance, following the prescribed initial conditions detailed in Section 4.1. This disc is embedded within a low-density circumstellar medium that provides a uniform background across the computational domain. At $t = 0\,\mathrm{d}$, both the radial and vertical velocity components are initialised to zero, while the azimuthal component follows the Keplerian profile described in Section 4.1.

The emergence of outflowing material is first observed in $t = 16\,\mathrm{d}$ (see Figure 5.2, left column). The density distribution at this stage reveals the formation of a compact, dome-shaped bubble in the innermost regions, reaching an altitude of approximately $z \approx 0.3 \times 10^{15}\,\mathrm{cm}$. This feature originates near the inner boundary, where the infalling gas encounters a pressure barrier resulting from the numerical treatment of the central point mass. Consequently, the material is redirected vertically. The corresponding vertical velocity map confirms this behaviour; upward motion is intensely concentrated along the rotation axis ($R \approx 0$), where velocities reach the upper limit of the colourbar. Meanwhile, the rest of the domain remains largely undisturbed, and the disc mid-plane shows no signs of significant perturbation.

By $t = 33.5\,\mathrm{d}$, the outflow undergoes a rapid expansion, filling the inner half of the domain (Figure 5.2, centre column). The density morphology transitions into a distinctly turbulent regime, characterised by elongated features and irregular contrasts at the interface with the ambient medium. Such structures are indicative of Kelvin–Helmholtz instabilities, which are triggered by the significant velocity shear at the contact discontinuity between the high-velocity outflow and the slower surrounding gas. The vertical velocity field displays a clear radial gradient, with peak values maintained along the rotation axis and v_z gradually decreasing with increasing R. The outermost boundary of the outflow corresponds to the swept-up ambient gas, moving at more moderate velocities compared to the fast axial component. Throughout this expansion phase, the disc mid-plane continues to maintain its intact structure.

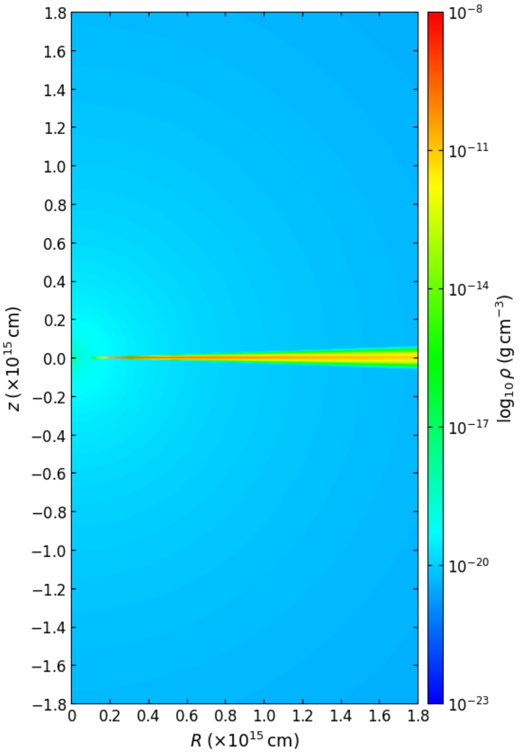

Figure 5.1: Logarithmic density map of the initial conditions at $t = 0\,\mathrm{d}$. The accretion disc is confined to the mid-plane ($z = 0$) and extends across the full radial extent of the domain. No outflow is present at this stage.

The final snapshot at $t = 137\,\mathrm{d}$ (Figure 5.2, right column) shows the system in a quasi-steady state. The outflow has filled most of the domain, and the turbulent structure present during the expansion phase has partially settled into a more uniform configuration.

A primary result of this simulation is that the accretion disc remains stable and geometrically thin over the entire evolution, demonstrating that the energy deposited into the surrounding medium is insufficient to disrupt the disc structure under these hydrodynamic conditions. The vertical velocity field retains its characteristic axial concentration, with elevated v_z values along the rotation axis from the inner boundary to the upper edge of the domain.

Since no magnetic field is present in this purely hydrodynamic simulation, the observed outflow takes the form of a pressure-driven bipolar wind rather than a magnetically collimated jet, with the axial concentration of v_z arising from the system geometry and the thermal pressure gradient driving material primarily along the rotation axis.

It should be noted that the extreme velocities visible near $R = 0$ at small z saturate the colourbar and are consistent with the velocity ceiling $v_{\mathrm{lim}} = 2.4 \times 10^{10}\,\mathrm{cm\,s^{-1}}$ enforced to prevent superluminal velocities near the point mass, as described in Section 4.1. These boundary-adjacent values should therefore be interpreted with caution and viewed as numerical artefacts rather than purely physical high-velocity components. The broader implications of neglecting explicit viscosity and magnetic

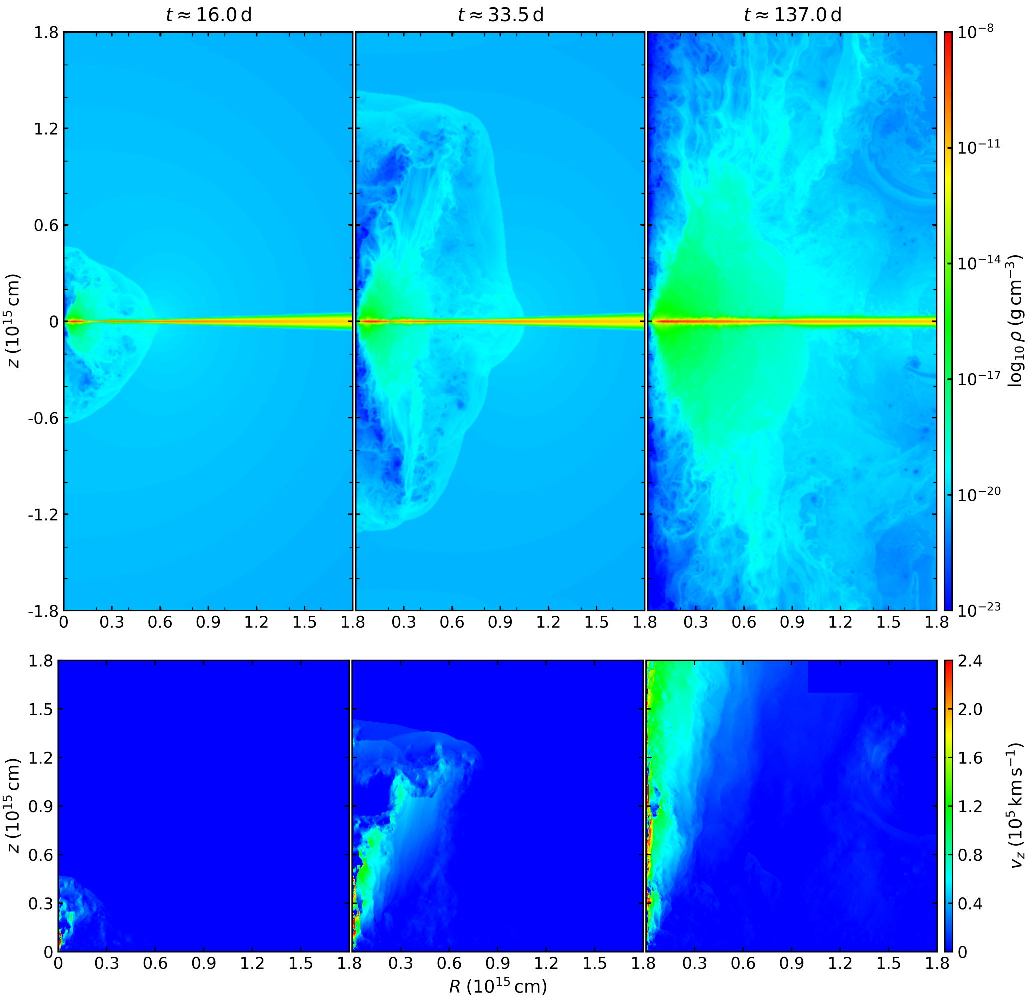

Figure 5.2: Time evolution of the 2D cylindrical hydrodynamic simulation. Top row: logarithmic density maps at $t = 16$, 33.5, and 137 d. Bottom row: corresponding vertical velocity v_z maps. The disc mid-plane remains intact throughout. The outflow transitions from a compact inner structure at $t = 16\,\mathrm{d}$ to a domain-filling bipolar wind by $t = 137\,\mathrm{d}$, with axially concentrated upward velocities evident throughout.

fields are further analysed in Chapter 6.

5.2 3D Cartesian MHD simulations

All visualisations of the three-dimensional simulations presented in this section were produced using the `VisIt` software package by extracting a two-dimensional slice of the three-dimensional data at $y = 0$, resulting in the xz-plane passing through the rotation axis.

5.2.1 Weak-field configuration

The initial setup of the weak-field simulation, shown in Figure 5.3, mirrors the geometrically thin accretion disc of the two-dimensional model, now implemented within a three-dimensional Cartesian domain. At $t = 0\,\mathrm{d}$, the radial and vertical velocity components are set to zero, whereas the azimuthal velocity profile follows the Keplerian profile described in Section 4.1.

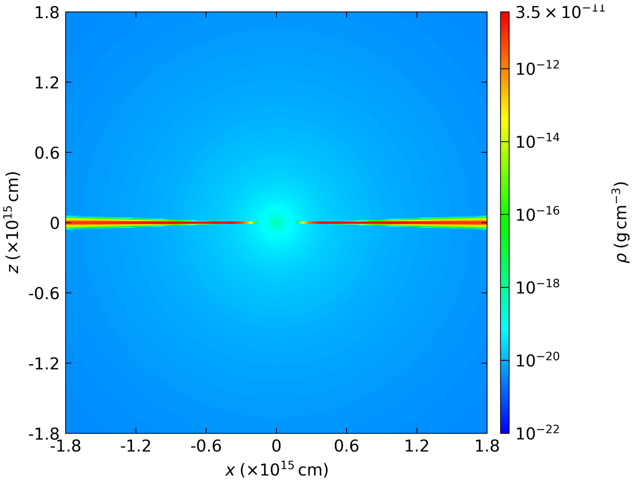

Figure 5.3: Logarithmic density map of the initial conditions at $t = 0\,\mathrm{d}$ for the weak-field ($B = 50\,\mathrm{G}$) 3D Cartesian MHD simulation, shown in the xz-plane.

The onset of evolution, captured at $t \approx 5.0\,\mathrm{d}$ in Figure 5.4, is marked by the development of a compact bipolar structure near the central object. In the density maps, this manifests as small, rounded lobes positioned symmetrically above and below the mid-plane. The apparent multi-lobe morphology is likely a numerical artefact of the dipole field interacting with the Cartesian grid, rather than an intrinsic physical instability. Vertical velocity maps at this epoch confirm that the emerging outflow remains confined to the central region, with only modest vertical velocities.

By $t \approx 9.5\,\mathrm{d}$, the outflow has expanded significantly, forming two prominent bipolar lobes that occupy the inner half of the computational domain. The density maps reveal low-density cavities within these lobes, surrounded by a denser shell of compressed material, consistent with a bubble expanding through the ambient medium. Velocity fields indicate that the gas within both lobes has reached the maximum of the displayed velocity range of $2.7 \times 10^5\,\mathrm{km\,s^{-1}}$. Furthermore, the northern lobe displays a complex, turbulent internal structure. Throughout this expansion, the disc mid-plane remains geometrically thin and intact.

Upon reaching a quasi-steady state at $t \approx 18.5\,\mathrm{d}$, the northern lobe has reached the upper domain boundary. Near the disc, the outflow assumes a conical geometry, with the highest velocities concentrated along the rotation axis. A notable asymmetry between the northern and southern hemispheres is observed, with the northern component being more extended. This asymmetry is a genuine three-dimensional effect, which cannot arise in the two-dimensional simulation due to its imposed axial symmetry. The disc mid-plane remains undisturbed for the duration of the simula-

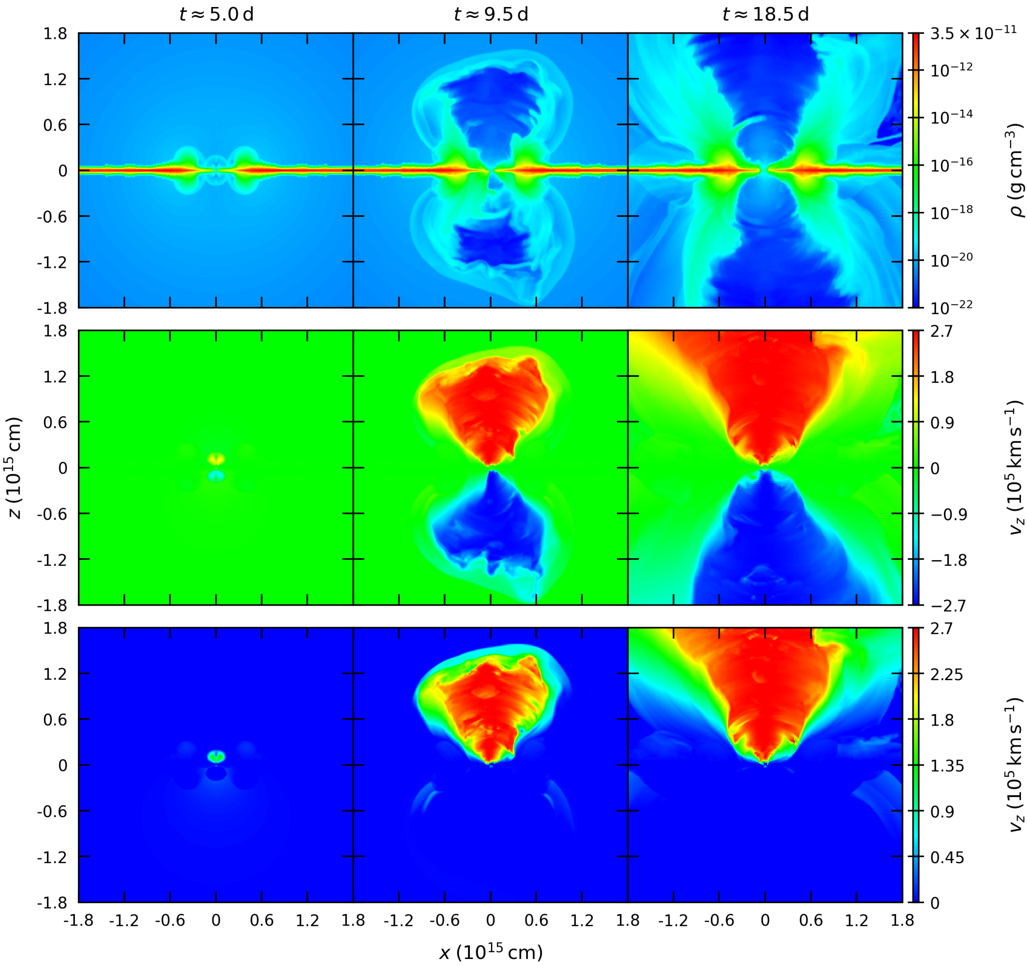

Figure 5.4: Time evolution of the weak-field ($B = 50\,\mathrm{G}$) 3D Cartesian MHD simulation, shown in the xz-plane. Top row: logarithmic density. Middle row: full bipolar vertical velocity v_z. Bottom row: upward component $v_z^+ \geq 0$ only, revealing the internal structure of the northern lobe.

tion. The character of the outflow is that of a wide-angle magnetised wind rather than a collimated jet.

The temperature distribution in quasi-steady state (Figure 5.5) shows a cold disc mid-plane consistent with the initial power-law profile. The cold disc is surrounded by a hot inner region where temperatures reach $10^{10} - 5 \times 10^{11}\,\mathrm{K}$ at the base of the outflow, mainly due to adiabatic compression. The outflowing lobes exhibit temperatures ranging from 10^9 to $10^{10}\,\mathrm{K}$, decreasing toward the periphery. Since the current numerical framework does not incorporate radiative cooling, these temperatures are likely to be overestimated compared to physical conditions, a limitation further addressed in Chapter 6.

To provide a quantitative assessment of the morphology of the fully developed outflow, the full opening angles of its individual component were estimated at $z = 0.6 \times 10^{15}\,\mathrm{cm}$. At this altitude, the jet structure is sufficiently established, while remaining relatively unaffected by instabilities in the domain. In this configuration, the outflow is characterised by a broad, high velocity spine with a full opening angle of approximately 80°. This core is enveloped by a significantly slower and wider layer (sheath) that spans approximately 101°. This multi-component transverse velocity profile is qualitatively consistent with the spine-sheath jet structures observed in ANG [Bruni et al., 2021].

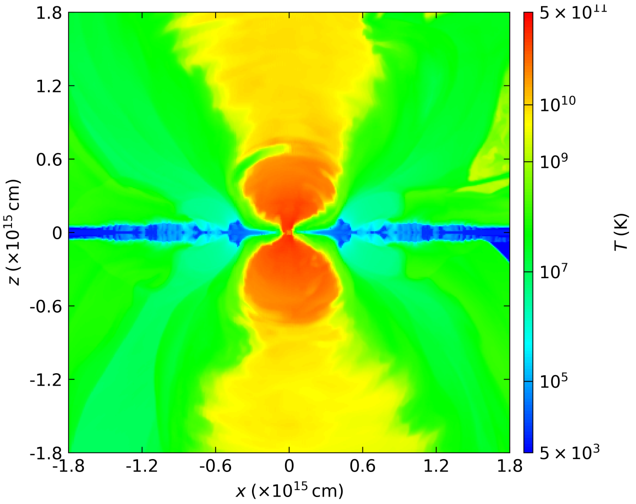

Figure 5.5: Logarithmic temperature map of the weak-field ($B = 50\,\mathrm{G}$) simulation at quasi-steady state ($t \approx 18.5\,\mathrm{d}$), shown in the xz-plane.

5.2.2 Mid-field configuration

The mid-field configuration employs a dipole moment of $m_1 = 1.668 \times 10^{38}\,\mathrm{erg\,G^{-1}}$, which corresponds to a magnetic field strength of $B = 100\,\mathrm{G}$ at the gravitational radius. This increased field strength leads to a higher Alfvén velocity within the disc, which significantly constrains the CFL time step. Consequently, the computational demand per unit of physical time is elevated, limiting the total simulated time for this configuration to approximately $9.0 \times 10^5\,\mathrm{s}$ (10.4 d). Despite this temporal limitation, the implications of which are further addressed in Chapter 6, the magnetised outflow successfully reaches the domain boundaries in both hemispheres, satisfying the quasi-steady criterion established in Section 4.2. The corresponding evolution of the density and vertical velocity fields is illustrated in Figure 5.6 at three representative times: $t \approx 5.0\,\mathrm{d}$, 7.4 d, and 10.4 d. At $t \approx 5.0\,\mathrm{d}$, a compact bipolar outflow is already established near the central object. At the same time, the inner regions of the disc exhibit vertical inflation driven by the increasing magnetic pressure. The density morphology at this stage displays the same characteristic multi-lobe pattern as in the weak-field case at a comparable stage. As previously analysed in Section 5.2.1, this structure is considered a numerical artefact arising from the interaction between the dipole field geometry and the Cartesian grid. The recurrence of this pattern across different field strengths reinforces this interpretation. At this early stage, the vertical velocity field indicates a relatively weak upward motion, primarily concentrated close to the central object.

By $t \approx 7.4\,\mathrm{d}$, the system undergoes a rapid dynamical transition. The domain becomes dominated by two large, rounded outflow lobes extending to approximately $z \approx \pm 1.5 \times 10^{15}\,\mathrm{cm}$. The interiors of these lobes are characterised by low-density cavities, where the density drops below $\sim 10^{-21}\,\mathrm{g\,cm^{-3}}$. Turbulent filaments of denser material are observed extending into these cavities, suggesting the onset of hydrodynamical instabilities at the interface between the outflow and the ambient medium. The vertical velocity field reaches approximately $2.7 \times 10^5\,\mathrm{km\,s^{-1}}$ throughout the majority of the volume of the northern lobe. A slight hemispheric asymmetry is already detectable, as the northern lobe appears to be more extended than the southern one.

The simulation reaches a quasi-steady state by $t \approx 10.4\,\mathrm{d}$, at which point the northern lobe has encountered the upper domain boundary. While the internal turbulent structures within the lobes increase in complexity, the overall bipolar morphology remains stable. The accretion disc mid-plane remains intact and geometrically thin throughout the entire run. Similarly to the weak-field case, the outflow does not exhibit significant spatial collimation and takes the form of a wide-angle magnetised wind. The thermal properties of the quasi-steady state are shown in Figure 5.7. The temperature distribution follows the same pattern described for the weak-field case: the disc mid-plane remains cold ($T < 10^5\,\mathrm{K}$), while a hot inner zone forms at the base of the outflow, reaching temperatures of approximately $5 \times 10^{11}\,\mathrm{K}$. The outflowing lobes maintain temperatures between 10^9 and $10^{10}\,\mathrm{K}$, with a gradual decline toward the outer boundaries. As before, the absence of radiative cooling in *CASTRO*

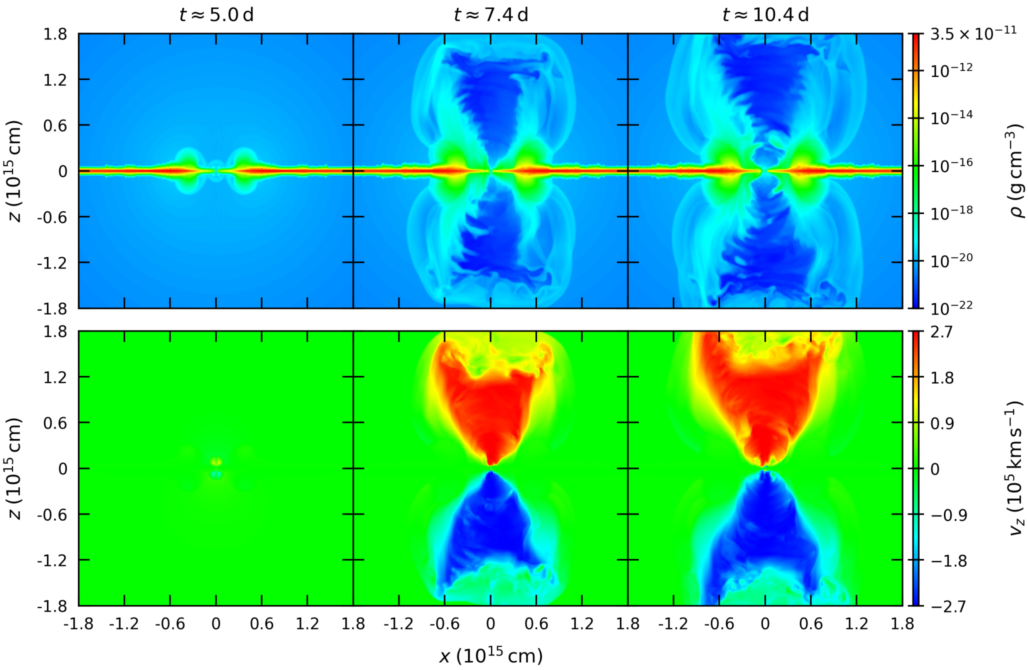

Figure 5.6: Time evolution of the mid-field ($B = 100\,\mathrm{G}$) 3D Cartesian MHD simulation, shown in the xz-plane. Top row: logarithmic density maps. Bottom row: corresponding vertical velocity v_z maps. The disc mid-plane remains intact throughout. The outflow transitions from a compact central structure at $t \approx 5.0\,\mathrm{d}$ to a domain-filling bipolar wind by $t \approx 10.4\,\mathrm{d}$.

implies that these temperatures are overestimated relative to physical conditions, a point further addressed in Chapter 6.

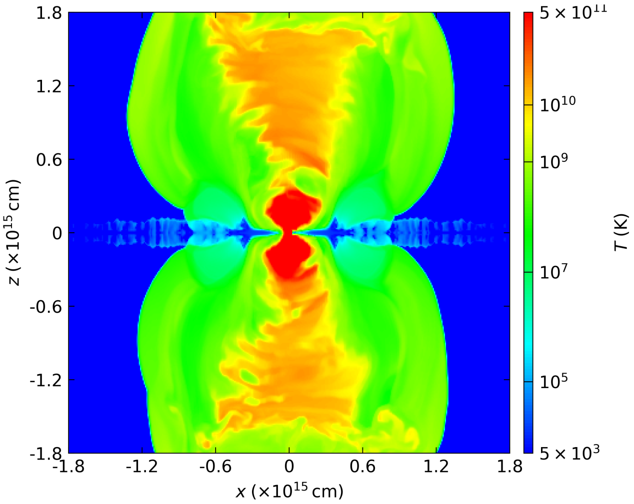

Figure 5.7: Logarithmic temperature map of the mid-field ($B = 100\,\mathrm{G}$) simulation at quasi-steady state ($t \approx 10.4\,\mathrm{d}$), shown in the xz-plane.

5.2.3 Strong-field configuration

The strong-field simulation uses a dipole moment of $m_1 = 3.336 \times 10^{38}\,\mathrm{erg\,G^{-1}}$, corresponding to a magnetic field strength of $B = 200\,\mathrm{G}$ at the gravitational radius. As observed in the mid-field configuration (Section 5.2.2), the elevated Alfvén velocity imposes a more severe constraint on the CFL time step, limiting the total simulated physical time to approximately $3.1 \times 10^5\,\mathrm{s}$ ($\approx 3.6\,\mathrm{d}$). Despite this temporal restriction, the magnetised outflow reaches the domain boundaries in both hemispheres before the conclusion of the run, thereby satisfying the quasi-steady criterion established in Section 4.2.

The temporal evolution of the density and vertical velocity fields is illustrated in Figure 5.8 at three representative times: $t \approx 1.45\,\mathrm{d}$, $t \approx 2.78\,\mathrm{d}$, and $t \approx 3.59\,\mathrm{d}$. At $t \approx 1.45\,\mathrm{d}$, the density morphology exhibits the characteristic multi-lobe structure previously described in Section 5.2.1, which is attributed to the interaction between the dipole field geometry and the Cartesian grid discretisation. At this stage, the vertical velocity remains confined to the innermost regions with amplitudes significantly below the colourbar maximum, while the disc mid-plane remains undisturbed.

By $t \approx 2.78\,\mathrm{d}$, the outflow has expanded, forming large bipolar lobes that occupy a large portion of the computational domain. Low-density cavities are clearly visible within these lobes, and the vertical velocity field saturates the colour scale throughout the majority of the outflow volume. A hemispheric asymmetry between the northern and southern lobes is present, consistent with the inherent three-dimensional effects identified in Section 5.2.1. By $t \approx 3.59\,\mathrm{d}$, the outflow has reached the domain boundaries in both hemispheres. It maintains a conical geometry in the vicinity of the disc, with peak velocities concentrated along the rotation axis. The disc mid-plane remains geometrically thin and undisturbed throughout the simulation. As with the weak- and mid-field cases, the outflow manifests itself as a wide-angle magnetised wind.

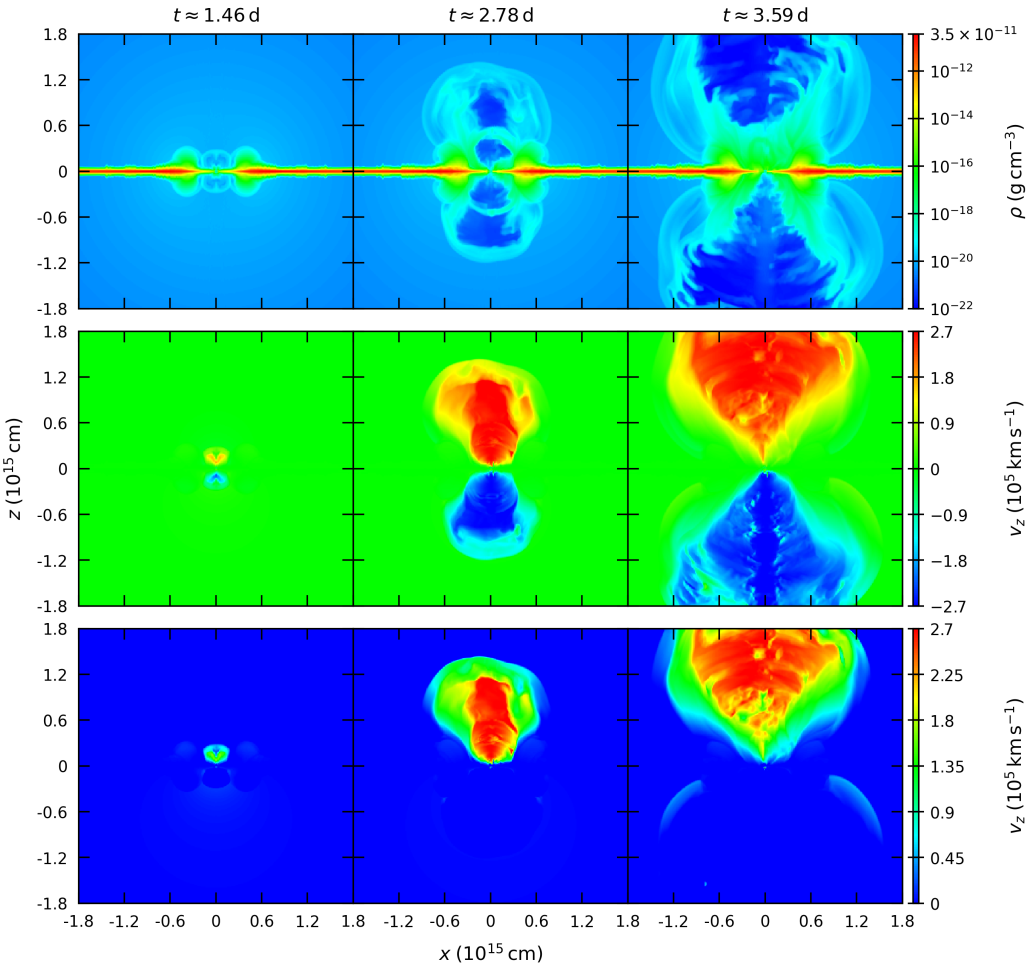

Figure 5.8: Time evolution of the strong-field ($B = 200\,\mathrm{G}$) 3D Cartesian MHD simulation, shown in the xz-plane. Top row: logarithmic density maps. Middle row: full bipolar vertical velocity v_z. Bottom row: upward component $v_z^+ \geq 0$ only, revealing the internal structure of the northern lobe.

The spatial distribution of the magnetic field magnitude is presented in Figure 5.9 at $t \approx 2.08\,\mathrm{d}$, $t \approx 2.78\,\mathrm{d}$, and $t \approx 3.47\,\mathrm{d}$. At $t \approx 2.08\,\mathrm{d}$, the field is primarily localised within the inner outflow lobes, with the amplitude decreasing sharply with radial distance from the central object. Beyond the inner quarter of the domain, the field strength drops to negligible values. By $t \approx 2.78\,\mathrm{d}$, the magnetic field has been advected outward by the expanding wind, occupying a significant portion of the domain, while the peak amplitude in the innermost region has declined as the magnetic flux is redistributed over a growing volume. By $t \approx 3.47\,\mathrm{d}$, the field occupies the full extent of the outflow lobes and exhibits structured filamentary patterns, likely associated with the turbulent dynamics of the magnetised expansion.

Using the same approach as in the weak-field case, the opening angles of the

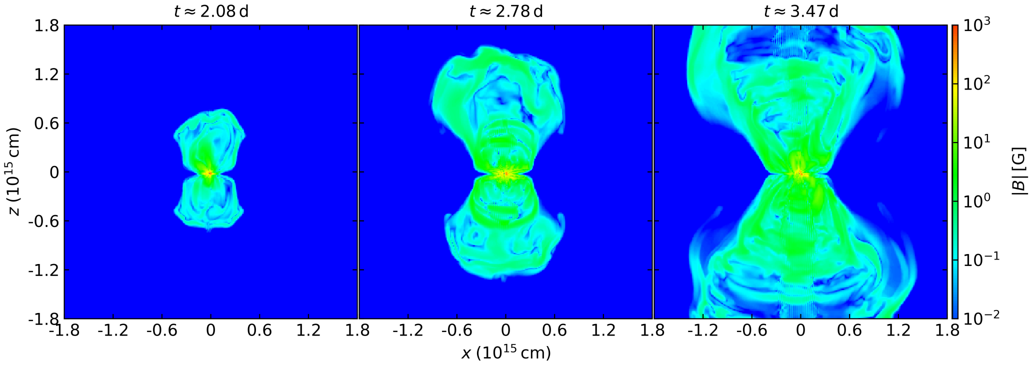

Figure 5.9: Logarithmic distribution of the magnetic field magnitude $|B|$ for the strong-field ($B = 200\,\mathrm{G}$) simulation in the xz-plane at $t \approx 2.08\,\mathrm{d}$ (left), $t \approx 2.78\,\mathrm{d}$ (centre), and $t \approx 3.47\,\mathrm{d}$ (right). The field is initially confined to the innermost regions and is progressively advected outward by the expanding magnetised wind. The regular stripes visible along the rotation axis in the centre and right panels are a numerical artefact arising from the interpolation of the dipole field onto the Cartesian grid.

outflow components were measured at the reference height of $z = 0.6 \times 10^{15}$ cm. The presence of a stronger magnetic field ($B = 200\,\mathrm{G}$) results in a noticeably stronger collimation of the high-velocity central region. Specifically, the full opening angle of the spine is reduced to approximately 51°, representing a significant narrowing compared to the $\approx 80°$ observed in the weak-field simulation. In contrast, the surrounding slower sheath maintains a relatively wide profile with an opening angle of approximately 97°. These results suggest that the increased magnetic field strength and the associated hoop stresses act primarily on the fast central spine, while the outer sheath remains less affected by such collimation [Bruni et al., 2021].

5.3 Radiative transfer: spectral energy distributions

5.3.1 Angle-resolved spectra

The angle-resolved spectral energy distributions (SEDs) for the quasi-steady-state snapshots across all three magnetic field configurations are presented in Figure 5.10. Each panel compares the emission along the polar axis ($\mu = \cos\theta = 0.95$), which corresponds to the jet direction, with the radiation extracted near the equatorial plane ($\mu = -0.05$). The raw Monte Carlo output, shown as thin translucent lines, shows significant sampling noise that increases toward longer wavelengths. A Savitzky-Golay smoothing filter was applied to each spectrum. The resulting curves are shown as thick lines. The wavelength range is truncated at 4000 Å, beyond which the data are dominated by noise.

All three configurations exhibit spectra that rise sharply toward the lower boundary of the computational grid at $\lambda \approx 150$ Å, which lies in the extreme ultraviolet

(EUV) regime. The polar spectra appear to peak at or below this limit. This suggests that the primary emission from the polar outflow region is concentrated in the soft X-ray band, outside the wavelength range of the present calculation. In contrast, the equatorial spectra reach their maximum between 250 and 300 Å. This spectral shift reflects the lower effective temperatures associated with the accretion disc surface compared to the high-temperature plasma in the polar regions.

In the weak-field case ($B = 50\,\mathrm{G}$, $t \approx 18.5\,\mathrm{d}$), the polar flux exceeds the equatorial emission throughout the EUV band. This excess decreases with increasing wavelength, and the spectra converge beyond the Lyman limit (912 Å). This distribution is consistent with the thermal structure discussed in Section 5.2.1, where the highest temperatures are found at the base of the outflow along the rotation axis. The mid-field configuration ($B = 100\,\mathrm{G}$, $t \approx 10.4\,\mathrm{d}$) follows a qualitatively similar pattern, with the two spectra becoming comparable in the UV and optical bands.

A distinct behaviour is observed in the strong-field configuration ($B = 200\,\mathrm{G}$, $t \approx 3.6\,\mathrm{d}$), where the equatorial spectrum remains consistently brighter than the polar one across the entire simulated wavelength range. This inversion of the directional flux ratio, relative to the weaker field models, represents a qualitative change in the angular radiation pattern. The physical implications of this reversal, as well as the impact of the shorter integration time for the mid-field model, are further analysed in Chapter 6.

Videos of the temporal evolution of the density and velocity fields for all simulations are provided in the Appendix B.

5.3.2 Jet luminosity

To evaluate the angular distribution of the radiation field, we extracted the bolometric luminosity L_{bol} from the *SEDONA* output as a function of the viewing angle. These calculations were performed for each magnetic field configuration in the quasi-steady state. The resulting values are shown in Figure 5.11 and are summarised in Table 5.1.

All three configurations show a consistent trend in which the polar directions are significantly more luminous than the equatorial plane. As shown in Table 5.1, the polar-to-equatorial luminosity ratios range from approximately 9 to 17. This enhancement results from the magnetised outflow geometry described in Section 4.2. The low-density polar cavities allow radiation to escape with less resistance along the rotation axis. In contrast, equatorial radiation is suppressed by the optically thicker accretion disc.

The degree of hemispheric symmetry varies between configurations. The weak-field and mid-field cases remain relatively symmetric with $L_{\mathrm{S}}/L_{\mathrm{N}}$ ratios of 1.24 and 0.92, respectively. However, the strong-field configuration shows a pronounced asymmetry in which the southern pole is roughly three times brighter than the northern pole. This difference is consistent with the structural variations between the outflow lobes shown in Section 5.2.3 and indicates that the three-dimensional effects are significant in the strong-field regime.

The bolometric results for the strong-field case might seem to contradict the

Table 5.1: Bolometric luminosities extracted from *SEDONA* at quasi-steady state for each field configuration. $L_{\rm S}$ and $L_{\rm N}$ denote the south- and north-polar luminosities ($\cos\theta = -0.95$ and $+0.95$ respectively), and $L_{\rm eq}$ is the mean of the two equatorial viewing angles closest to $\cos\theta = 0$. The final column gives the south-polar luminosity as a fraction of the Eddington luminosity $L_{\rm Edd} = 5.0 \times 10^{44}$ erg s^{-1} for $M_\bullet = 4 \times 10^6\, M_\odot$. The weak-field, mid-field, and strong-field configurations correspond to $B = 50$, 100, and 200 G respectively.

Configuration	$L_{\rm S}$ [erg s^{-1}]	$L_{\rm N}$ [erg s^{-1}]	$L_{\rm eq}$ [erg s^{-1}]	$L_{\rm S}/L_{\rm eq}$	$L_{\rm N}/L_{\rm eq}$	$L_{\rm S}/L_{\rm Edd}$
Weak-field	1.91×10^{44}	1.53×10^{44}	1.42×10^{43}	13.4	10.8	0.38
Mid-field	2.66×10^{42}	2.88×10^{42}	2.96×10^{41}	9.0	9.7	0.005
Strong-field	2.46×10^{43}	8.11×10^{42}	1.39×10^{42}	17.6	5.8	0.049

findings in Section 5.3.1. In that section, the equatorial spectrum appeared brighter than the polar one within the range of 150 to 4000 Å. We can resolve this apparent contradiction by considering the peak of the polar emission. The polar flux in the strong-field model decreases monotonically from the short-wavelength boundary of the grid at 150 Å. This suggests that the majority of the polar radiation is emitted in the soft X-ray band, which is outside the plotted range. Because $L_{\rm bol}$ integrates over the entire frequency grid of the simulation, the polar direction remains the most luminous overall. The spectral inversion discussed previously represents a shift in how energy is distributed across different bands rather than a change in the total energy output.

Absolute luminosities vary between models. The weak-field case reaches $L_{\rm S} = 1.91 \times 10^{44}$ erg s^{-1}, which is about 0.38 of the Eddington luminosity. The mid-field and strong-field values are lower by one to two orders of magnitude. We discuss the physical causes of these differences and the influence of integration times in Chapter 6.

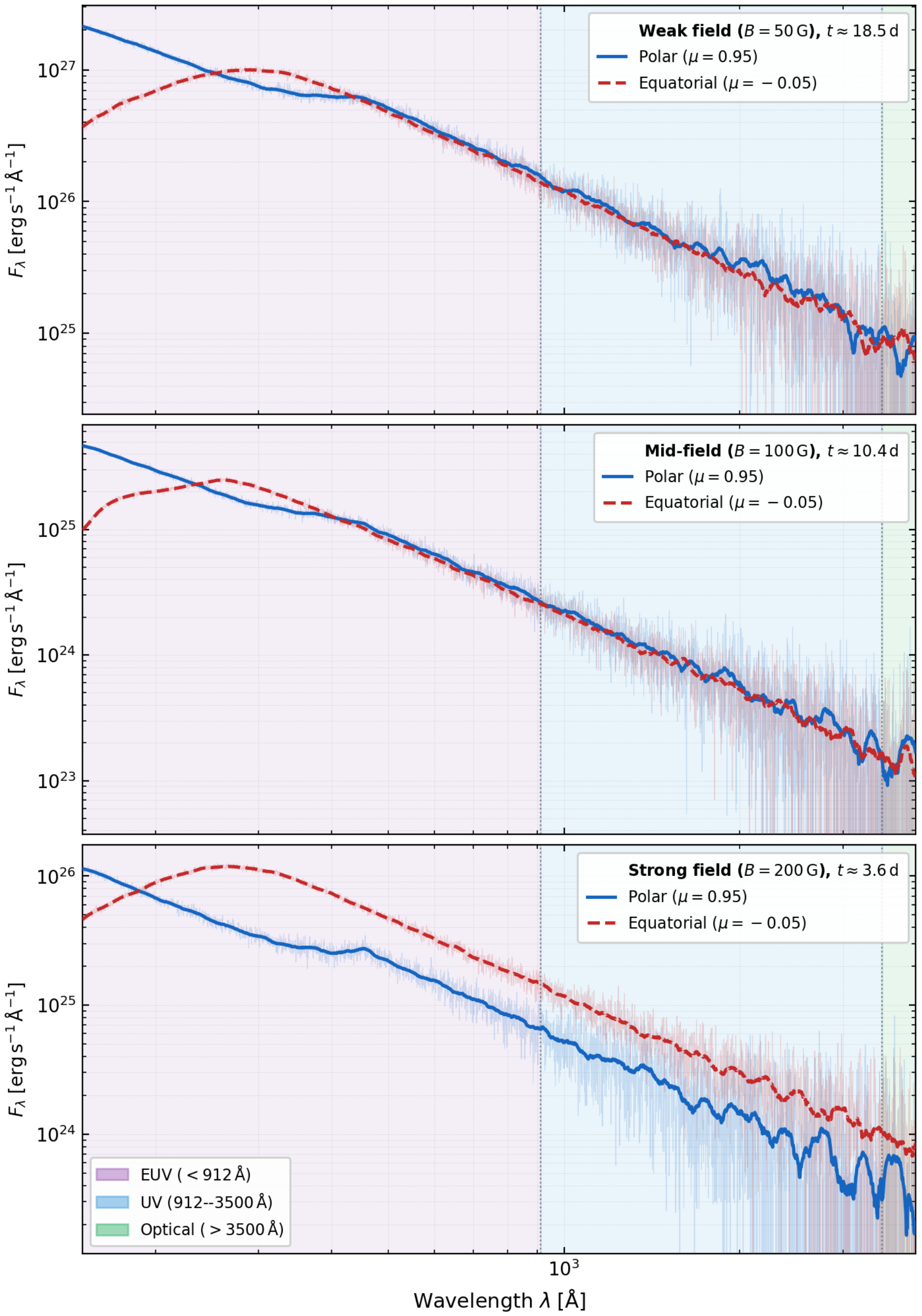

Figure 5.10: Angle-resolved spectral energy distributions from *SEDONA* for the weak-field ($B = 50\,\mathrm{G}$, $t \approx 18.5\,\mathrm{d}$), mid-field ($B = 100\,\mathrm{G}$, $t \approx 10.4\,\mathrm{d}$), and strong-field ($B = 200\,\mathrm{G}$, $t \approx 3.6\,\mathrm{d}$) configurations (top to bottom). Solid blue: polar spectrum ($\mu = 0.95$); red dashed: equatorial ($\mu = -0.05$). Thin translucent lines show raw Monte Carlo output; thick lines show Savitzky-Golay smoothed spectra. Coloured bands indicate EUV ($\lambda < 912$ Å), UV (912–3500 Å), and optical (> 3500 Å) regions. The dotted vertical line marks the Lyman limit at 912 Å. The horizontal axis is logarithmic, with tick marks at integer multiples of 10^2 and 10^3 Å.

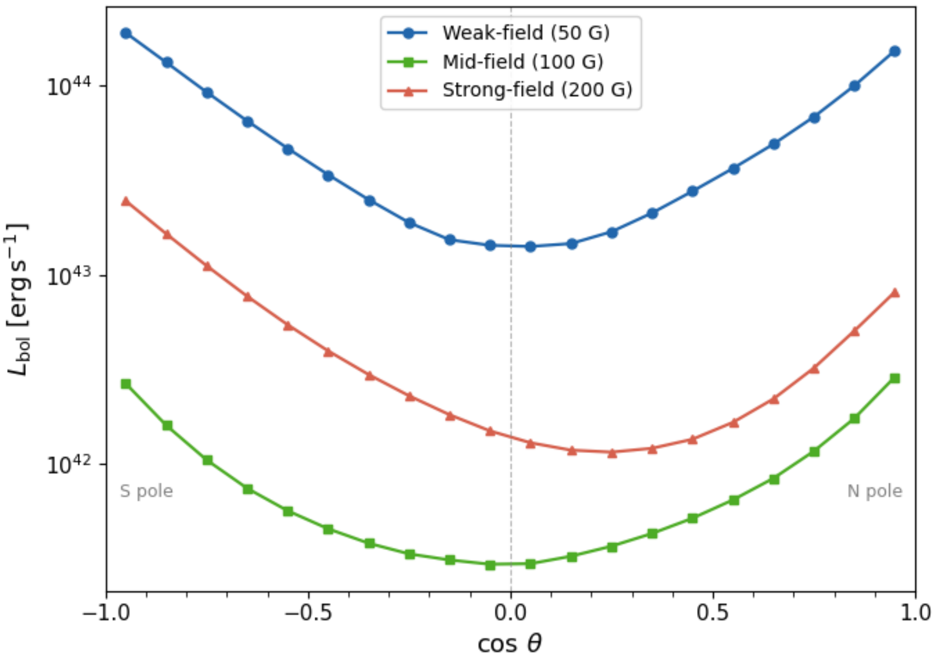

Figure 5.11: Bolometric luminosity $L_{\rm bol}$ as a function of viewing angle $\cos\theta$ for the weak-field ($B = 50\,{\rm G}$, $t \approx 18.5\,{\rm d}$), mid-field ($B = 100\,{\rm G}$, $t \approx 10.4\,{\rm d}$), and strong-field ($B = 200\,{\rm G}$, $t \approx 3.6\,{\rm d}$) configurations at quasi-steady state. The angular direction $\cos\theta = -0.95$ roughly corresponds to the southern pole while $\cos\theta = +0.95$ to the northern pole.

Chapter 6

Discussion

6.1 Numerical modelling approximations

The simulations presented in this thesis were designed to capture the main dynamical features of accretion onto a supermassive black hole within the capabilities of the *CASTRO* framework. Several approximations were adopted, and their implications are considered in this chapter.

The gravitational potential in both simulations follows the standard Newtonian point-mass form described in Sections A.3 and 3.1.4. This approach does not reproduce the ISCO at $r_{\mathrm{ISCO}} = 6\,r_{\mathrm{g}}$ found in the Schwarzschild spacetime, and therefore, the velocity structure in the vicinity of the central object should be interpreted with caution. The Paczyński–Wiita potential [Paczyński and Wiita, 1980] would provide a closer approximation to the relativistic inner boundary at a comparable computational cost and represents a natural improvement for future work.

Angular momentum transport in the two-dimensional simulation is governed by the numerical viscosity inherent to the PPM solver rather than by an explicit physical prescription. The Shakura–Sunyaev parameter $\alpha = 0.1$ enters only the initial conditions, where it determines the ratio between the azimuthal and radial velocity components at the disc base, as described in Section 4.1, and does not drive the later evolution. In the three-dimensional MHD simulations, the angular momentum is instead carried by magnetic stresses. Because the *CASTRO* MHD solver is not available for cylindrical coordinates, a Cartesian grid must be used for the MHD runs. The interaction of the dipole field geometry with the Cartesian discretisation produces a characteristic multi-lobe density morphology in the early frames. This multi-lobe structure is a numerical artefact rather than a physical instability, as discussed in Section 5.2.1.

Radiative cooling is absent from all *CASTRO* runs. Temperatures that reach 5×10^{11} K at the base of the outflow in the three-dimensional simulations are therefore likely overestimated relative to physical conditions. This directly affects the *SEDONA* post-processing, as the inflated temperature field increases the emitted luminosity, so the resulting spectra and bolometric luminosities should be regarded as upper estimates rather than precise predictions. The three MHD configurations also differ in their total simulated physical time. The mid-field and strong-field runs are shorter than the weak-field run by factors of approximately 1.8 and 5, respectively. This is because higher Alfvén velocities in the stronger-field cases impose a more severe constraint on the time step through the CFL condition.

6.2 Interpretation of luminosity and spectral results

The bolometric luminosities extracted from *SEDONA* differ by more than two orders of magnitude between the three field configurations. This ordering cannot be attributed to field strength alone, because the mid-field case produces the lowest absolute luminosity despite running for an intermediate time of 10.4 d. The most likely explanation is that the different integration times are the primary driver, as the weak-field simulation ran for 18.5 d, giving the outflow more time to develop and fill the low-density polar cavities through which radiation escapes most freely, while the strong-field case covered only 3.6 d. A definitive separation of the effects of field strength and integration time would require extending all three runs to a common physical time, which was not possible within the computational budget of this work.

In the strong-field configuration, the equatorial spectrum is brighter than the polar spectrum throughout the wavelength range shown in Figure 5.10. This does not mean that the polar direction is less luminous overall. The polar flux decreases monotonically from the short-wavelength boundary of the *SEDONA* grid at 150 Å. This indicates that the dominant polar emission falls in the soft X-ray band below this limit and is therefore absent from the spectral plot. The bolometric luminosities confirm that the polar direction remains the most luminous overall in all three configurations, since L_{bol} integrates over the full frequency grid.

The south-polar luminosity of the weak-field configuration reaches $L_{\mathrm{S}} = 1.91 \times 10^{44}\,\mathrm{erg\,s^{-1}}$, which corresponds to approximately $0.38\,L_{\mathrm{Edd}}$. For comparison, the observed quiescent bolometric luminosity of Sgr A* is approximately $10^{36}\,\mathrm{erg\,s^{-1}} \approx 10^{-9}\,L_{\mathrm{Edd}}$ [Event Horizon Telescope Collaboration et al., 2022], which is eight orders of magnitude lower. This difference is expected, as Sgr A* accretes at an extremely low rate through a radiatively inefficient flow [Frank et al., 2002], whereas the simulations here are initialised with a sub-Eddington thin-disc profile at a much higher accretion rate. In this point, it would be interesting and desirable for future work to calculate corresponding models for much larger jet extensive lengths and compare them with the assumed Galactic jet luminosity of the past active jet of $10^{42}\,\mathrm{erg\,s^{-1}}$ [cf. Kurfürst et al., 2025]. However, these values should be carefully verified through further calculations using other radiative transfer codes in parallel, and in particular, alternative massively parallel codes that allow for the implementation of general relativity effects within MHD calculations, such as HARM [Gammie et al., 2003], Athena++ [Stone et al., 2020], or others.

Chapter 7

Summary and Conclusions

This thesis has presented a numerical study of accretion onto a supermassive black hole of mass $M_\bullet = 4 \times 10^6\,M_\odot$. Using the *CASTRO* radiation-hydrodynamics code, a series of simulations were performed, including a two-dimensional cylindrical hydrodynamic model and three three-dimensional Cartesian magnetohydrodynamic (MHD) configurations with varying magnetic field strengths. The radiative properties of the resulting outflows were subsequently computed with the Monte Carlo radiative transfer code *SEDONA*, applied to snapshots extracted at or near the quasi-steady state of each simulation.

In the two-dimensional cylindrical hydrodynamic simulation, the accretion disc remains geometrically thin and dynamically stable over the full duration of the simulated time. The disc mid-plane remains undisturbed by the outflowing material at all stages of the evolution. A pressure-driven, wide-angle bipolar wind develops from the inner boundary region, driven by the thermal pressure gradient in the absence of a magnetic field. The concentration of vertical velocity along the rotation axis suggests that the outflow geometry is primarily determined by the cylindrical symmetry of the system rather than magnetic collimation.

The three-dimensional MHD simulations were carried out for weak-field ($B = 50\,\mathrm{G}$), mid-field ($B = 100\,\mathrm{G}$), and strong-field ($B = 200\,\mathrm{G}$) configurations. In all three cases, the formation of a magnetised bipolar outflow has been confirmed. During the early evolution, all cases show a characteristic multi-lobe density morphology arising from the interaction of the Cartesian grid with the magnetic dipole geometry. The long-term evolution demonstrated persistent bipolar outflows characterised by low-density polar cavities, while the disc mid-plane remains intact. The strong-field configuration exhibits a hemispheric asymmetry in the outflow structure, suggesting that three-dimensional effects become increasingly significant at higher field strengths.

The angle-resolved spectral energy distributions computed by *SEDONA* confirm a clear dependence of the emitted radiation on the viewing angle. In the weak-field and mid-field configurations, the polar flux exceeds the equatorial throughout the EUV band, and both spectra rise steeply towards the short-wavelength limit of the computational domain. This indicates that the dominant polar emission resides within the soft X-ray band. The equatorial spectra peak in the EUV regime, reflecting the lower effective temperatures of the disc surface. In the strong-field configuration, although the equatorial flux appears brighter within the simulated spectral range, bolometric luminosity calculations confirm that the polar direction remains the primary outlet for energy output. This apparent inversion is explained by the fact that the majority of the polar emission is shifted toward the soft X-ray regime, falling below the short-wavelength boundary of the computational grid.

Future work should address the approximations discussed in Chapter 6. A primary objective would be the implementation of the Paczyński–Wiita potential to better approximate the relativistic inner boundary compared to a Newtonian point-mass potential. Incorporating an explicit radiative cooling function would additionally improve the thermal structure of the outflow and reduce the overestimation of temperatures in the polar regions. Finally, extending all three MHD configurations to a common physical time would provide a more direct comparison of the effect of magnetic field strength on the bolometric luminosity and spectral properties.

Bibliography

M. A. Abramowicz and P. C. Fragile. Foundations of Black Hole Accretion Disk Theory. *Living Reviews in Relativity*, 16:1, 2013. doi: 10.12942/lrr-2013-1.

A. S. Almgren, V. E. Beckner, J. B. Bell, M. S. Day, L. H. Howell, C. C. Joggerst, M. J. Lijewski, A. Nonaka, M. Singer, and M. Zingale. CASTRO: A New Compressible Astrophysical Solver. I. Hydrodynamics and Self-gravity. *The Astrophysical Journal*, 715:1221–1238, 2010. doi: 10.1088/0004-637X/715/2/1221.

J. M. Bardeen, W. H. Press, and S. A. Teukolsky. Rotating Black Holes: Locally Nonrotating Frames, Energy Extraction, and Scalar Synchrotron Radiation. *The Astrophysical Journal*, 178:347–370, 1972. doi: 10.1086/151796.

M. J. Berger and I. Rigoutsos. An Algorithm for Point Clustering and Grid Generation. *IEEE Transactions on Systems, Man, and Cybernetics*, 21(5):1278–1286, 1991. doi: 10.1109/21.120081.

R. D. Blandford and D. G. Payne. Hydromagnetic flows from accretion discs and the production of radio jets. *Monthly Notices of the Royal Astronomical Society*, 199:883–903, 1982. doi: 10.1093/mnras/199.4.883.

R. D. Blandford and R. L. Znajek. Electromagnetic extraction of energy from Kerr black holes. *Monthly Notices of the Royal Astronomical Society*, 179:433–456, 1977. doi: 10.1093/mnras/179.3.433.

G. Bruni, J. L. Gómez, L. Vega-García, A. P. Lobanov, et al. RadioAstron reveals a spine-sheath jet structure in 3C 273. *Astronomy & Astrophysics*, 654:A27, 2021. doi: 10.1051/0004-6361/202039423.

P. Colella and P. R. Woodward. The Piecewise Parabolic Method (PPM) for Gas-Dynamical Simulations. *Journal of Computational Physics*, 54:174–201, 1984. doi: 10.1016/0021-9991(84)90143-8.

Event Horizon Telescope Collaboration, Kazunori Akiyama, et al. First Sagittarius A* Event Horizon Telescope Results. I. The Shadow of the Supermassive Black Hole in the Center of the Milky Way. *The Astrophysical Journal Letters*, 930:L12, 2022. doi: 10.3847/2041-8213/ac6674.

J. Frank, A. King, and D. J. Raine. *Accretion Power in Astrophysics*. Cambridge University Press, Cambridge, 3rd edition, 2002. ISBN 0521629578.

Charles F. Gammie, Jonathan C. McKinney, and Gábor Tóth. HARM: A Numerical Scheme for General Relativistic Magnetohydrodynamics. *ApJ*, 589(1):444–457, May 2003. doi: 10.1086/374594.

Gravity Collaboration, R. Abuter, A. Amorim, M. Bauböck, J. P. Berger, H. Bonnet, W. Brandner, Y. Clénet, V. C. Du Foresto, P. T. De Zeeuw, J. Dexter, G. Duvert, A. Eckart, F. Eisenhauer, N. M. Förster Schreiber, P. Garcia, F. Gao, E. Gendron, R. Genzel, O. Gerhard, S. Gillessen, M. Habibi, X. Haubois, T. Henning, S. Hippler, M. Horrobin, A. Jiménez-Rosales, L. Jocou, P. Kervella, S. Lacour, V. Lapeyrère, J.-B. Le Bouquin, P. Léna, T. Ott, T. Paumard, K. Perraut, G. Perrin, O. Pfuhl, S. Rabien, G. Rodriguez Coira, G. Rousset, S. Scheithauer, A. Sternberg, O. Straub, C. Straubmeier, E. Sturm, L. J. Tacconi, F. Vincent, S. von Fellenberg, I. Waisberg, F. Widmann, E. Wieprecht, E. Wiezorrek, J. Woillez, and S. Yazici. A geometric distance measurement to the Galactic Center black hole with 0.3% uncertainty. *Astronomy & Astrophysics*, 625:L10, 2019. doi: 10.1051/0004-6361/201935656.

David J. Griffiths. *Introduction to Electrodynamics.* Cambridge University Press, 4th edition, 2017. ISBN 978-1-108-42041-9.

Daniel Kasen, R. C. Thomas, and P. Nugent. Time-dependent Monte Carlo Radiative Transfer Calculations for Three-dimensional Supernova Spectra, Light Curves, and Polarization. *The Astrophysical Journal*, 651:366–380, 2006. doi: 10.1086/506190.

M. P. Katz, A. Almgren, M. Barrios Sazo, K. Eiden, K. Gott, A. Harpole, J. M. Sexton, D. E. Willcox, W. Zhang, and M. Zingale. Preparing Nuclear Astrophysics for Exascale. In *Proceedings of the International Conference for High Performance Computing, Networking, Storage and Analysis (SC20)*, 2020. doi: 10.1109/SC41405.2020.00095.

R. P. Kerr. Gravitational Field of a Spinning Mass as an Example of Algebraically Special Metrics. *Physical Review Letters*, 11:237–238, 1963. doi: 10.1103/PhysRevLett.11.237.

Petr Kurfürst, Michal Zajaček, Norbert Werner, and Jiří Krtička. Red giant-jet collisions in galactic nuclei I: 3D hydrodynamical model of a few stellar orbits. *MNRAS*, 540(2):1586–1607, June 2025. doi: 10.1093/mnras/staf810.

P. Kurfürst. *Models of hot star decretion disks.* PhD thesis, Masaryk University, Faculty of Science, Brno, Czech Republic, 2015.

P. Kurfürst, A. Feldmeier, and J. Krtička. Time-dependent modeling of extended thin decretion disks of critically rotating stars. *Astronomy & Astrophysics*, 569: A23, 2014. doi: 10.1051/0004-6361/201424272.

L. D. Landau and E. M. Lifshitz. *Fluid Mechanics*, volume 6 of *Course of Theoretical Physics.* Pergamon Press, Oxford, 2nd edition, 1987.

Joseph M. Michail, Farhad Yusef-Zadeh, Mark Wardle, Devaky Kunneriath, Joseph L. Hora, Howard Bushouse, Giovanni G. Fazio, Sera Markoff, and Howard A. Smith. Multiwavelength observations of Sgr A*. II. 2019 July 21 and 26. *ApJ*, 971:52, 2024. doi: 10.3847/1538-4357/ad5332.

D. Mihalas and B. W. Mihalas. *Foundations of Radiation Hydrodynamics*. Oxford University Press, New York, 1984.

G. H. Miller and P. Colella. A Conservative Three-Dimensional Eulerian Method for Coupled Solid-Fluid Shock Capturing. *Journal of Computational Physics*, 183: 26–82, 2002. doi: 10.1006/jcph.2002.7158.

I. F. Mirabel and L. F. Rodríguez. Sources of Relativistic Jets in the Galaxy. *Annual Review of Astronomy and Astrophysics*, 37:409–443, 1999. doi: 10.1146/annurev.astro.37.1.409.

J. R. Oppenheimer and H. Snyder. On Continued Gravitational Contraction. *Physical Review*, 56:455–459, 1939. doi: 10.1103/PhysRev.56.455.

B. Paczyński and P. J. Wiita. Thick accretion disks and supercritical luminosities. *Astronomy and Astrophysics*, 88:23–31, 1980.

J. E. Pringle. Accretion discs in astrophysics. *Annual Review of Astronomy and Astrophysics*, 19:137–162, 1981. doi: 10.1146/annurev.aa.19.090181.001033.

R. A. Remillard and J. E. McClintock. X-Ray Properties of Black-Hole Binaries. *Annual Review of Astronomy and Astrophysics*, 44:49–92, 2006. doi: 10.1146/annurev.astro.44.051905.092532.

Sean M. Ressler, Christopher J. White, Eliot Quataert, and James M. Stone. Ab initio horizon-scale simulations of magnetically arrested accretion in Sagittarius A* fed by stellar winds. *ApJL*, 896:L6, 2020. doi: 10.3847/2041-8213/ab9532.

K. Schwarzschild. Über das Gravitationsfeld eines Massenpunktes nach der Einsteinschen Theorie. *Sitzungsberichte der Königlich Preußischen Akademie der Wissenschaften*, pages 189–196, 1916.

N. I. Shakura and R. A. Sunyaev. Black holes in binary systems. Observational appearance. *Astronomy and Astrophysics*, 24:337–355, 1973.

James M. Stone, Kengo Tomida, Christopher J. White, and Kyle G. Felker. The Athena++ Adaptive Mesh Refinement Framework: Design and Magnetohydrodynamic Solvers. *ApJS*, 249(1):4, July 2020. doi: 10.3847/1538-4365/ab929b.

W. Zhang, A. Almgren, V. Beckner, J. Bell, J. Blaschke, C. Chan, M. Day, B. Friesen, K. Gott, D. Graves, M. Katz, A. Myers, T. Nguyen, A. Nonaka, M. Rosso, S. Williams, and M. Zingale. AMReX: A framework for block-structured adaptive mesh refinement. *Journal of Open Source Software*, 4(37):1370, 2019. doi: 10.21105/joss.01370.

Appendix A

Basic equations and hydrodynamics

A.1 Differential operators in cylindrical polar coordinates

A.1.1 Cylindrical polar coordinates

The accretion disc can be described in a cylindrical coordinate system (R, ϕ, z), where R denotes the radial distance from the rotation axis, φ is the azimuthal angle, and z is the coordinate along the rotation axis, with $z = 0$ defining the disc midplane [Kurfürst, 2015]. Transformation equations from cylindrical to Cartesian coordinates are

$$x = R\cos\phi, \quad y = R\sin\phi, \quad z = z. \tag{A.1}$$

Assume the basis vectors of the system are $\hat{\boldsymbol{R}}$, $\hat{\boldsymbol{\phi}}$, and $\hat{\boldsymbol{z}}$. Then, the transformation equations of the basis vectors from Cartesian to cylindrical coordinates are:

$$\hat{\boldsymbol{R}} = \hat{\boldsymbol{x}}\cos\phi + \hat{\boldsymbol{y}}\sin\phi, \quad \hat{\boldsymbol{\phi}} = -\hat{\boldsymbol{x}}\sin\phi + \hat{\boldsymbol{y}}\cos\phi, \quad \hat{\boldsymbol{z}} = \hat{\boldsymbol{z}}. \tag{A.2}$$

Here $\hat{\boldsymbol{x}}$, $\hat{\boldsymbol{y}}$, and $\hat{\boldsymbol{z}}$ are Cartesian basis unit vectors. The inverse transformations from cylindrical to Cartesian basis are

$$\hat{\boldsymbol{x}} = \hat{\boldsymbol{R}}\cos\phi - \hat{\boldsymbol{\phi}}\sin\phi, \quad \hat{\boldsymbol{y}} = \hat{\boldsymbol{R}}\sin\phi + \hat{\boldsymbol{\phi}}\cos\phi, \quad \hat{\boldsymbol{z}} = \hat{\boldsymbol{z}}. \tag{A.3}$$

In contrast to Cartesian basis vectors, $\hat{\boldsymbol{z}}$ is the only constant basis vector in the cylindrical polar system. The time and spatial non-zero derivatives of the unit vectors are

$$\frac{\partial\hat{\boldsymbol{R}}}{\partial\phi} = \hat{\boldsymbol{\phi}}, \quad \frac{\partial\hat{\boldsymbol{\phi}}}{\partial\phi} = -\hat{\boldsymbol{R}}, \quad \frac{\partial\hat{\boldsymbol{R}}}{\partial t} = \dot{\phi}\,\hat{\boldsymbol{\phi}}, \quad \frac{\partial\hat{\boldsymbol{\phi}}}{\partial t} = -\dot{\phi}\,\hat{\boldsymbol{R}}, \quad \frac{\partial\hat{\boldsymbol{z}}}{\partial t} = 0. \tag{A.4}$$

A.1.2 Differential operators

Before stating the hydrodynamic equations, we establish the relevant differential operators in cylindrical polar coordinates, which describe the geometric curvature of the coordinate system and are essential for the correct formulation of conservation laws [Kurfürst, 2015]. Assuming a scalar field $f(R, \phi, z)$, its gradient, which gives the direction and rate of maximum spatial variation of the quantity f, is given by

$$\vec{\nabla} f = \hat{\boldsymbol{R}} \frac{\partial f}{\partial R} + \hat{\boldsymbol{\phi}} \frac{1}{R} \frac{\partial f}{\partial \phi} + \hat{\boldsymbol{z}} \frac{\partial f}{\partial z}. \tag{A.5}$$

Assuming a vector field $\vec{A}(R, \phi, z)$, its divergence in cylindrical coordinates is given by

$$\vec{\nabla} \cdot \vec{A} = \frac{1}{R} \frac{\partial}{\partial R}(R A_R) + \frac{1}{R} \frac{\partial A_\phi}{\partial \phi} + \frac{\partial A_z}{\partial z}. \tag{A.6}$$

The curl of a vector field $\vec{A} = A_R \, \hat{\boldsymbol{R}} + A_\phi \, \hat{\boldsymbol{\phi}} + A_z \, \hat{\boldsymbol{z}}$ in cylindrical coordinates is

$$\vec{\nabla} \times \vec{A} = \left(\frac{1}{R} \frac{\partial A_z}{\partial \phi} - \frac{\partial A_\phi}{\partial z} \right) \hat{\boldsymbol{R}} + \left(\frac{\partial A_R}{\partial z} - \frac{\partial A_z}{\partial R} \right) \hat{\boldsymbol{\phi}} + \frac{1}{R} \left[\frac{\partial}{\partial R}(R A_\phi) - \frac{\partial A_R}{\partial \phi} \right] \hat{\boldsymbol{z}}. \tag{A.7}$$

Lastly, we define the Laplacian operator in cylindrical coordinates as

$$\Delta = \vec{\nabla} \cdot \vec{\nabla} = \frac{1}{R} \frac{\partial}{\partial R} \left(R \frac{\partial}{\partial R} \right) + \frac{1}{R^2} \frac{\partial^2}{\partial \phi^2} + \frac{\partial^2}{\partial z^2}. \tag{A.8}$$

A.2 Velocity and acceleration in cylindrical coordinates

Using the transformation equations above, we define the position and velocity vector in cylindrical coordinates, respectively, as [Kurfürst, 2015]

$$\vec{r} = R \hat{\boldsymbol{R}} + z \hat{\boldsymbol{z}}, \qquad \vec{V} = \frac{\mathrm{d}\vec{r}}{\mathrm{d}t} = \dot{R} \hat{\boldsymbol{R}} + \dot{\phi} R \hat{\boldsymbol{\phi}} + \dot{z} \hat{\boldsymbol{z}}. \tag{A.9}$$

By definition, the velocity and acceleration vectors can be written as

$$\vec{V} = V_R \, \hat{\boldsymbol{R}} + V_\phi \, \hat{\boldsymbol{\phi}} + V_z \, \hat{\boldsymbol{z}}, \qquad \vec{a} = \frac{\mathrm{d}\vec{V}}{\mathrm{d}t} = a_R \, \hat{\boldsymbol{R}} + a_\phi \, \hat{\boldsymbol{\phi}} + a_z \, \hat{\boldsymbol{z}}. \tag{A.10}$$

By differentiating (A.9) with respect to time, we obtain the components of the acceleration vector

$$a_R = \ddot{R} - R\dot{\phi}^2 = \frac{\mathrm{d}V_R}{\mathrm{d}t} - R\dot{\phi}^2, \qquad a_\phi = R\ddot{\phi} + 2\dot{R}\dot{\phi} = \frac{\mathrm{d}V_\phi}{\mathrm{d}t} + \dot{R}\dot{\phi}, \qquad a_z = \ddot{z} = \frac{\mathrm{d}V_z}{\mathrm{d}t}. \tag{A.11}$$

Using the identity $\mathrm{d}/\mathrm{d}t = \partial/\partial t + \vec{V} \cdot \vec{\nabla}$, we can rewrite the acceleration components in terms of the velocity field as

$$a_R = \frac{\partial V_R}{\partial t} + V_R \frac{\partial V_R}{\partial R} + \frac{V_\phi}{R} \frac{\partial V_R}{\partial \phi} + V_z \frac{\partial V_R}{\partial z} - \frac{V_\phi^2}{R}, \tag{A.12}$$

$$a_\phi = \frac{\partial V_\phi}{\partial t} + V_R \frac{\partial V_\phi}{\partial R} + \frac{V_\phi}{R} \frac{\partial V_\phi}{\partial \phi} + V_z \frac{\partial V_\phi}{\partial z} + \frac{V_R V_\phi}{R}, \tag{A.13}$$

$$a_z = \frac{\partial V_z}{\partial t} + V_R \frac{\partial V_z}{\partial R} + \frac{V_\phi}{R} \frac{\partial V_z}{\partial \phi} + V_z \frac{\partial V_z}{\partial z}. \tag{A.14}$$

The last term in Eq. (A.12) expresses the centrifugal acceleration induced by azimuthally directed rotation, and the last term in Eq. (A.13) represents half of the Coriolis acceleration, with the remaining half absorbed into the advection terms $(\vec{V}\cdot\vec{\nabla})V_R$ and $(\vec{V}\cdot\vec{\nabla})V_\phi$, respectively.

A.3 Gravitational potential

The gravitational field of the central object plays a fundamental role in determining the structure and dynamics of the accretion disc. For a central mass $M_\bullet$ treated as a point mass, the Newtonian gravitational potential at a position (R, z) in cylindrical coordinates is given by [Kurfürst, 2015]

$$\Phi(R,z) = -\frac{GM_\bullet}{(R^2+z^2)^{1/2}}, \tag{A.15}$$

where G is the gravitational constant. In the disc midplane ($z = 0$), the potential reduces to $\Phi(R) = -GM_\bullet/R$, and the corresponding radial gravitational acceleration is

$$g_R = -\frac{\partial\Phi}{\partial R} = -\frac{GM_\bullet}{R^2}. \tag{A.16}$$

For a test particle in a circular orbit, the gravitational acceleration is balanced by the centrifugal term V_ϕ^2/R. Setting these equal defines the Keplerian velocity, [Kurfürst et al., 2014, Kurfürst, 2015]

$$V_K = \sqrt{\frac{GM_\bullet}{R}}, \tag{A.17}$$

which represents the azimuthal velocity of a particle in a stable circular orbit under Newtonian gravity. The corresponding Keplerian angular velocity is $\Omega_K = V_K/R = \sqrt{GM_\bullet/R^3}$, consistent with the definition introduced in Section 2.4.

The purely Newtonian potential is, however, insufficient when modelling accretion onto a black hole, since it does not reproduce the key relativistic features of the Schwarzschild spacetime, such as the existence of an ISCO. A widely used approximation that captures these effects without requiring a full general relativistic treatment is the pseudo-Newtonian potential [Paczyński and Wiita, 1980, Abramowicz and Fragile, 2013]

$$\Phi_{\mathrm{PW}}(r) = -\frac{GM_\bullet}{r-r_{\mathrm{s}}}, \tag{A.18}$$

where $r = (R^2+z^2)^{1/2}$ is the spherical radial distance from the central object and r_{s} is the Schwarzschild radius. The potential diverges at $r = r_{\mathrm{s}}$, mimicking the behaviour of the event horizon. Despite its simple form, the Paczyński-Wiita potential correctly reproduces the location of the ISCO at $r = 3r_{\mathrm{s}}$, the marginally bound orbit at $r = 2r_{\mathrm{s}}$, and the specific energies of circular orbits within approximately ten per cent of the values predicted by general relativity. These properties make it a standard tool in numerical simulations of black hole accretion.

In the simulations presented in this thesis, the standard Newtonian point-mass potential is implemented within the *CASTRO* code as the gravitational source term.

Although the Paczyński-Wiita potential would better approximate the relativistic environment near the black hole, the Newtonian treatment is adopted here as a first approximation.

A.4 Cauchy stress tensor

The stress tensor describes the internal forces acting within a fluid. For a Newtonian fluid that exhibits a linear relation between the rate of strain and the shear stresses, the stress tensor may be written as [Landau and Lifshitz, 1987]

$$T_{ij} = -P\delta_{ij} + \sigma_{ij}, \tag{A.19}$$

where P is the scalar thermal pressure, δ_{ij} is the Kronecker delta, and σ_{ij} is the symmetric viscous stress tensor. For a Newtonian fluid, σ_{ij} takes the form [Kurfürst, 2015]

$$\sigma_{ij} = \eta\left(\nabla_i V_j + \nabla_j V_i\right) + \left(\zeta - \frac{2}{3}\eta\right)\nabla_k V^k\,\delta_{ij}, \tag{A.20}$$

where η is the dynamic viscosity coefficient and ζ is the bulk viscosity coefficient. The kinematic viscosity ν is related to the dynamic viscosity by

$$\nu = \frac{\eta}{\rho}. \tag{A.21}$$

In cylindrical coordinates, the independent components of the stress tensor are

$$T_{RR} = -P + 2\eta\left(\frac{\partial V_R}{\partial R}\right) + \left(\zeta - \frac{2}{3}\eta\right)\vec{\nabla}\cdot\vec{V}, \tag{A.22}$$

$$T_{\phi\phi} = -P + 2\eta\left(\frac{1}{R}\frac{\partial V_\phi}{\partial \phi} + \frac{V_R}{R}\right) + \left(\zeta - \frac{2}{3}\eta\right)\vec{\nabla}\cdot\vec{V}, \tag{A.23}$$

$$T_{zz} = -P + 2\eta\left(\frac{\partial V_z}{\partial z}\right) + \left(\zeta - \frac{2}{3}\eta\right)\vec{\nabla}\cdot\vec{V}, \tag{A.24}$$

$$T_{R\phi} = \eta\left[\frac{1}{R}\frac{\partial V_R}{\partial \phi} + R\frac{\partial}{\partial R}\left(\frac{V_\phi}{R}\right)\right], \tag{A.25}$$

$$T_{Rz} = \eta\left(\frac{\partial V_z}{\partial R} + \frac{\partial V_R}{\partial z}\right), \tag{A.26}$$

$$T_{\phi z} = \eta\left(\frac{1}{R}\frac{\partial V_z}{\partial \phi} + \frac{\partial V_\phi}{\partial z}\right). \tag{A.27}$$

Appendix B

Simulation videos

Videos of the evolution toward the quasi-steady state for all simulations are available online. Each video covers the full development from the initial conditions to the quasi-steady configuration; the quasi-steady criterion is defined in Section 4.2.

2D cylindrical hydrodynamic simulation

Variable	Description	Link
$\log_{10}\rho$	Logarithmic density evolution, Rz-plane	Video 1
v_z	Vertical velocity evolution, Rz-plane	Video 2

Table B.1: Videos of the 2D cylindrical hydrodynamic simulation ($t = 0$ to quasi-steady state at $t \approx 137\,\mathrm{d}$).

3D Cartesian MHD simulations

Configuration	B [G]	Variable	Description	Link
Weak-field	50	$\log_{10}\rho$	Density, xz-plane	Video 3
Weak-field	50	v_z	Full bipolar velocity, xz-plane	Video 4
Weak-field	50	v_z^+	Upward component only, xz-plane	Video 5
Mid-field	100	$\log_{10}\rho$	Density, xz-plane	Video 6
Mid-field	100	v_z	Full bipolar velocity, xz-plane	Video 7
Strong-field	200	$\log_{10}\rho$	Density, xz-plane	Video 8
Strong-field	200	v_z	Full bipolar velocity, xz-plane	Video 9
Strong-field	200	v_z^+	Upward component only, xz-plane	Video 10

Table B.2: Videos of the 3D Cartesian MHD simulations for the weak-field ($t \approx 0$–$18.5\,\mathrm{d}$), mid-field ($t \approx 0$–$10.4\,\mathrm{d}$), and strong-field ($t \approx 0$–$3.6\,\mathrm{d}$) configurations.